

NO-A187 710

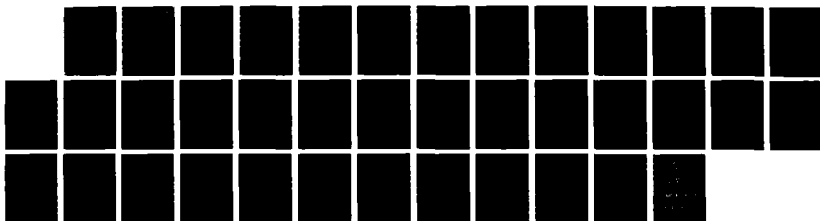
NUMERICAL SIMULATIONS OF THE WAKE DOWNSTREAM OF A
TWIN-SCREW DESTROYER MODEL(U) NAVAL RESEARCH LAB
WASHINGTON DC T F SWEAN 11 DEC 87 NRL-MR-6131

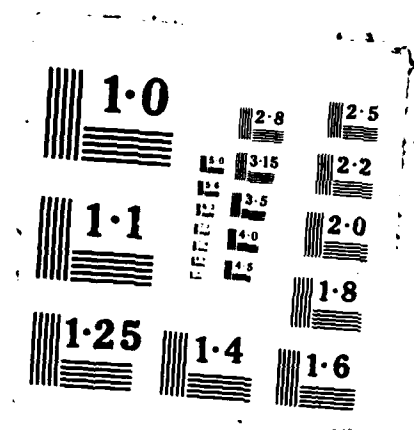
1/1

UNCLASSIFIED

F/G 28/4

NL





Naval Research Laboratory

Washington, DC 20375-5000

DTIC FILE 6001



2

NRL Memorandum Report 6131

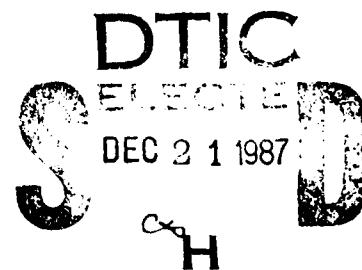
AD-A187 710

Numerical Simulations of the Wake Downstream of a Twin-Screw Destroyer Model

T. F. SWEAN, JR.

*Center for Hydrodynamics Developments
Laboratory for Computational Physics and Fluid Dynamics*

December 11, 1987



Approved for public release; distribution unlimited.

87 12 16 000

SECURITY CLASSIFICATION OF THIS PAGE

REPORT DOCUMENTATION PAGE				Form Approved OMB No 0704-0188	
1a. REPORT SECURITY CLASSIFICATION UNCLASSIFIED			1b. RESTRICTIVE MARKINGS A187710		
2a. SECURITY CLASSIFICATION AUTHORITY			3. DISTRIBUTION / AVAILABILITY OF REPORT		
2b. DECLASSIFICATION / DOWNGRADING SCHEDULE			Approved for public release; distribution unlimited.		
4. PERFORMING ORGANIZATION REPORT NUMBER(S) NRL Memorandum Report 6131			5. MONITORING ORGANIZATION REPORT NUMBER(S)		
6a. NAME OF PERFORMING ORGANIZATION Naval Research Laboratory		6b. OFFICE SYMBOL (If applicable)	7a. NAME OF MONITORING ORGANIZATION Office of Naval Research		
6c. ADDRESS (City, State, and ZIP Code) Washington, DC 20375-5000			7b. ADDRESS (City, State, and ZIP Code) Arlington, VA 22217		
8a. NAME OF FUNDING / SPONSORING ORGANIZATION Office of Naval Research		8b. OFFICE SYMBOL (If applicable) OCNR 017FB	9. PROCUREMENT INSTRUMENT IDENTIFICATION NUMBER		
8c. ADDRESS (City, State, and ZIP Code) Washington, DC 20375-5000			10. SOURCE OF FUNDING NUMBERS		
			PROGRAM ELEMENT NO. 62111N	PROJECT NO.	TASK NO. RU11W 71 801
					WORK UNIT ACCESSION NO DN156-264
11. TITLE (Include Security Classification) Numerical Simulations of the Wake Downstream of a Twin-Screw Destroyer Model					
12. PERSONAL AUTHOR(S) Swean, T. F., Jr.					
13a. TYPE OF REPORT Interim		13b. TIME COVERED FROM 1/87 TO 6/87		14. DATE OF REPORT (Year, Month, Day) 1987 December 11	
15. PAGE COUNT 38					
16. SUPPLEMENTARY NOTATION					
17. COSATI CODES			18. SUBJECT TERMS (Continue on reverse if necessary and identify by block number)		
FIELD	GROUP	SUB-GROUP			
			Turbulent ship wake ; Finite-element calculations ;		
			Self-propelled wake ;		
19. ABSTRACT (Continue on reverse if necessary and identify by block number)					
<p>The parabolic, incompressible, time-averaged Navier-Stokes equations together with a two-equation (K-ε) model of turbulence are used to numerically simulate the turbulent wake behind a self-propelled model of a twin-screw destroyer. Experimental data are employed to initialize the fluid state in a transverse plane 10.0 ft downstream of the stern from which point the wake evolution is computed to a plane 30.0 ft downstream. Two propeller operating conditions are considered, outboard propeller rotation and inboard propeller rotation. In the outboard simulation, the propeller thrust is bifurcated into upper and lower regions, the former of which eventually is convected to the free surface where the upwelling displaces the drag wake to outboard. This evolution combined with locally high levels of turbulence kinetic energy results in high transverse strain and transverse Reynolds stress in the surface region. In the inboard simulation the thrust wake remains unimodal and spatially stationary within the local transverse plane. Initial and small levels of velocity excess near the wake centerline quickly dissipate as the port and starboard drag wakes merge into a single diffuse velocity deficit structure. This results in considerably smaller transverse strain than in the outboard rotation simulation.</p>					
20. DISTRIBUTION / AVAILABILITY OF ABSTRACT <input checked="" type="checkbox"/> UNCLASSIFIED/UNLIMITED <input type="checkbox"/> SAME AS RPT <input type="checkbox"/> DTIC USERS			21. ABSTRACT SECURITY CLASSIFICATION UNCLASSIFIED		
22a. NAME OF RESPONSIBLE INDIVIDUAL Thomas F. Swean, Jr.			22b. TELEPHONE (Include Area Code) 202-767-2114		22c. OFFICE SYMBOL Code 4430

DD Form 1473, JUN 86

Previous editions are obsolete

SECURITY CLASSIFICATION OF THIS PAGE

CONTENTS

1. INTRODUCTION	1
2. DESCRIPTION OF EXPERIMENTS	1
3. INITIALIZATION OF TWAKE	2
4. RESULTS OF THE SIMULATIONS	4
5. COMPARISON AND FINAL REMARKS	8
6. ACKNOWLEDGMENTS	9
7. REFERENCES	10

Accession For	
NTIS GRA&I	<input checked="checked" type="checkbox"/>
DTIC TAB	<input type="checkbox"/>
Unannounced	<input type="checkbox"/>
Justification	
By	
Institution /	
Availability Codes	
Availability	
Date	
A-1	

NUMERICAL SIMULATIONS OF THE WAKE DOWNSTREAM OF A TWIN-SCREW DESTROYER MODEL

1. INTRODUCTION

The purpose of this report is to present and discuss the results of numerical simulations of high speed surface ship model experiments which have recently been conducted at the David W. Taylor Naval Ship Research and Development Center (DTNSRDC). In these experiments the turbulent wake behind a self-propelled model of a twin-screw destroyer was documented. Data from two of the experiments were forwarded to the Naval Research Laboratory (NRL) for the purpose of determining the accuracy with which such flow fields can be numerically simulated by means of three-dimensional marching codes. These data were used to generate initial conditions for calculations with the NRL code TWAKE. In the sections that follow brief descriptions of the experiments and the procedures for initializing the computations are given. The results of the simulations are then presented and discussed. Comparisons of the calculations and experiments have not been presented herein pending the release of the experimental results.

2. DESCRIPTION OF EXPERIMENTS

Experiments were conducted to determine the three dimensional turbulent velocity field and the free surface elevations in the wake region of a high speed surface ship model. A line drawing of the model is contained in Fig. 1 and Table 1 displays relevant data on the model dimensions and towing conditions.

A rectangular coordinate system fixed to the model was chosen to define the measurement locations. The origin of the coordinate system is at the intersection of the undisturbed free surface, the ship aft perpendicular (AP), and the vertical plane running down the ship longitudinal centerline (Fig. 2a). The "X" or streamwise axis is directed aft (positive direction) from the origin and in the model centerline plane. The "Y" or transverse axis is directed to starboard from the origin. The "Z" or vertical axis is directed upward to complete the orthogonal, right-handed coordinate system.

Mean velocity and turbulence measurements were taken using both laser doppler velocimetry (LDV) and hot-film anemometry (HF) techniques. Details of the instrumentation, procedures, and data reduction may be found in Ref. [1]. The measurement domain consisted of a series of vertical ($Y-Z$) planes at various axial locations in the wake. A schematic of the typical experimental cross-plane including the major wake producing elements of the model is shown in Fig. 2b. Generally the sensors were placed at a specified depth (Z) and measurements were taken point by point at intervals of 2.0 in in the range $-3.0 \leq Y \leq 33.0$. The measurement interval in the Z direction was also 2.0 in from -1.6 in (nearest to the free surface) to a maximum depth of between -17.0 in to -28.0 in depending on the distance aft of the model. At a few axial

locations the port half-plane was measured to check the symmetry of the flow field. The LDV tests yielded data for the three components of mean velocity, $(\bar{U}, \bar{V}, \bar{W})$, and the three turbulent normal stresses, which can be summed to give the total turbulence kinetic energy,

$$K = \frac{1}{2} (\overline{u'u'} + \overline{v'v'} + \overline{w'w'}) . \quad (1)$$

The LDV data were corrected for the wave orbital velocities. The cross-film sensors were employed in two orientations to yield independent realizations of the above mean flow and turbulence quantities as well as the two principal Reynolds stresses $(\overline{u'v'}, \overline{u'w'})$.

A matrix showing the scope of the measurements obtained is given in Table 2. The numbers in the table refer to the approximate number of points measured for a particular test which is characterized by

- 1) the distance from AP to the measurement plane,
- 2) the tow speed,
- 3) the rotation direction of the propellers (or unpropelled), and
- 4) the type sensor used for the measurements.

The elements denoted by an asterisk have been forwarded to NRL via Refs. [2-3].

Two of the data sets referenced in Table 2 have been used to develop initial conditions for the numerical simulations of the evolving wake flow fields. These are the 4.0 *knots* data at the 10.0 *ft* plane with both outboard (clockwise) and inboard (counter-clockwise) propeller rotation. The initialization process for TWAKE and a brief description of the simulation model are given in the next section.

3. INITIALIZATION OF TWAKE

The NRL code TWAKE is a suitably-modified derivative of the 3DPNS finite-element code described in Ref. [4]. The code solves the steady, three-dimensional, time-averaged (in the turbulence sense) parabolic Navier-Stokes equations. The effects of turbulence are described using modelled transport equations for the turbulence kinetic energy and the isotropic dissipation function, ϵ , along with an anisotropic closure for the turbulent stresses. For later reference the appropriate equation set is given below:

continuity:

$$\frac{\partial \bar{U}}{\partial X} + \frac{\partial \bar{V}}{\partial Y} + \frac{\partial \bar{W}}{\partial Z} = 0, \quad (2)$$

axial momentum:

$$\bar{U} \frac{\partial \bar{U}}{\partial X} + \bar{V} \frac{\partial \bar{U}}{\partial Y} + \bar{W} \frac{\partial \bar{U}}{\partial Z} = -\frac{1}{\rho_0} \frac{\partial P}{\partial X} - \frac{\partial (\overline{u'v'})}{\partial Y} - \frac{\partial (\overline{u'w'})}{\partial Z}, \quad (3)$$

vertical momentum:

$$\bar{U} \frac{\partial \bar{V}}{\partial X} + \bar{V} \frac{\partial \bar{V}}{\partial Y} + \bar{W} \frac{\partial \bar{V}}{\partial Z} = -\frac{1}{\rho_0} \frac{\partial P}{\partial Y} - \frac{\partial (\overline{v'w'})}{\partial X} - \frac{\partial (\overline{w'w'})}{\partial Z}, \quad (4)$$

transverse momentum:

$$\bar{U} \frac{\partial \bar{V}}{\partial X} + \bar{V} \frac{\partial \bar{V}}{\partial Y} + \bar{W} \frac{\partial \bar{V}}{\partial Z} = -\frac{1}{\rho_0} \frac{\partial P}{\partial Y} - \frac{\partial(\bar{v}'v')}{\partial Y} - \frac{\partial(\bar{v}'w')}{\partial Z}. \quad (5)$$

kinematic turbulent stresses:

$$\overline{u'u'} = C_1 K - C_2 C_4 \frac{K^3}{\epsilon^2} \left(\left(\frac{\partial \bar{U}}{\partial Y} \right)^2 + \left(\frac{\partial \bar{U}}{\partial Z} \right)^2 \right) - 2C_4 \frac{K^2}{\epsilon} \left(\frac{\partial \bar{U}}{\partial X} \right), \quad (6)$$

$$\overline{v'v'} = C_3 K - C_2 C_4 \frac{K^3}{\epsilon^2} \left(\frac{\partial \bar{U}}{\partial Y} \right)^2 - 2C_4 \frac{K^2}{\epsilon} \left(\frac{\partial \bar{V}}{\partial Y} \right), \quad (7)$$

$$\overline{w'w'} = C_3 K - C_2 C_4 \frac{K^3}{\epsilon^2} \left(\frac{\partial \bar{U}}{\partial Z} \right)^2 - 2C_4 \frac{K^2}{\epsilon} \left(\frac{\partial \bar{W}}{\partial Z} \right), \quad (8)$$

$$\overline{u'v'} = -C_4 \frac{K^2}{\epsilon} \left(\frac{\partial \bar{U}}{\partial Y} \right) - C_2 C_4 \frac{K^3}{\epsilon^2} \left(\frac{\partial \bar{U}}{\partial Z} \left(\frac{\partial \bar{V}}{\partial Z} + \frac{\partial \bar{W}}{\partial Y} \right) - 2 \frac{\partial \bar{U}}{\partial Y} \frac{\partial \bar{W}}{\partial Z} \right), \quad (9)$$

$$\overline{u'w'} = -C_4 \frac{K^2}{\epsilon} \left(\frac{\partial \bar{U}}{\partial Z} \right) - C_2 C_4 \frac{K^3}{\epsilon^2} \left(\frac{\partial \bar{U}}{\partial Y} \left(\frac{\partial \bar{V}}{\partial Z} + \frac{\partial \bar{W}}{\partial Y} \right) - 2 \frac{\partial \bar{U}}{\partial Z} \frac{\partial \bar{V}}{\partial Y} \right), \quad (10)$$

$$\overline{v'w'} = -C_4 \frac{K^2}{\epsilon} \left(\frac{\partial \bar{V}}{\partial Z} + \frac{\partial \bar{W}}{\partial Y} \right) - C_2 C_4 \frac{K^3}{\epsilon^2} \left(\frac{\partial \bar{U}}{\partial Y} \frac{\partial \bar{U}}{\partial Z} \right), \quad (11)$$

turbulence transport:

$$\bar{U} \frac{\partial K}{\partial X} + \bar{V} \frac{\partial K}{\partial Y} + \bar{W} \frac{\partial K}{\partial Z} = \frac{\partial}{\partial Y} \left(\frac{\nu_t}{\sigma_K} \frac{\partial K}{\partial Y} \right) + \frac{\partial}{\partial Z} \left(\frac{\nu_t}{\sigma_K} \frac{\partial K}{\partial Z} \right) + \mathcal{P} - \epsilon, \quad (12)$$

$$\bar{U} \frac{\partial \epsilon}{\partial X} + \bar{V} \frac{\partial \epsilon}{\partial Y} + \bar{W} \frac{\partial \epsilon}{\partial Z} = \frac{\partial}{\partial Y} \left(\frac{\nu_t}{\sigma_\epsilon} \frac{\partial \epsilon}{\partial Y} \right) + \frac{\partial}{\partial Z} \left(\frac{\nu_t}{\sigma_\epsilon} \frac{\partial \epsilon}{\partial Z} \right) + C_{\epsilon_1} \mathcal{P} \frac{\epsilon}{K} - C_{\epsilon_2} \frac{\epsilon^2}{K}, \quad (13)$$

where,

$$\mathcal{P} = -\overline{u'v'} \frac{\partial \bar{U}}{\partial Y} - \overline{u'w'} \frac{\partial \bar{U}}{\partial Z} - \overline{v'w'} \left(\frac{\partial \bar{V}}{\partial Z} + \frac{\partial \bar{W}}{\partial Y} \right) - (\overline{v'v'} - \overline{u'u'}) \frac{\partial \bar{V}}{\partial Y} - (\overline{w'w'} - \overline{u'u'}) \frac{\partial \bar{W}}{\partial Z}$$

and

$$\nu_t = C_4 \frac{K^2}{\epsilon}.$$

In its standard form the model contains the eight constants $\{C_1, C_2, C_3, C_4, \sigma_K, \sigma_\epsilon, C_{\epsilon_1}, C_{\epsilon_2}\}$ which take on the commonly accepted values $\{0.94, 0.067, 0.56, 0.068, 1.0, 1.3, 1.44, 1.92\}$. Cooper in Ref. [5] has considered variations in these values for flows near to a free surface. No adjustments were undertaken in the present study.

The above equation set describes an initial value problem that requires distributions of the three components of mean velocity, the turbulence kinetic energy, and the dissipation function in order to begin a computation. For the computations presented in this report the domain of Fig. 2b was modified to include the square region defined by $0.0 \leq Y \leq 36.0$ in and $-36.0 \leq Z \leq 0.0$ in. In this domain triangular finite elements

were constructed by connecting computational nodal points placed at 1.0 *in* intervals in both the *Y* and *Z* directions. This resulted in 1369 nodes and 2592 finite elements, a discretization approximately twice as dense as that used in the experiments.

For each simulation (outboard and inboard rotations at 4.0 *knots* beginning at the $X = 10.0$ *ft* plane) the LDV data for the mean velocity components and the vertical and streamwise turbulence normal stresses were linearly interpolated onto the computational grid. Due to the inherent difficulty in measuring the on-axis (Y') component of fluctuating velocity with the LDV system, the data for $\overline{v'v'}$ was not used. Rather, the turbulence kinetic energy was formed by adding twice the vertical normal stress to the streamwise normal stress. The dissipation function was assumed to be related to the turbulence kinetic energy through a dissipation length scale,

$$l_d = \frac{K^{3/2}}{\epsilon}. \quad (14)$$

The outboard rotation HF tests at 10.0 *ft* provided data for the principal components of Reynolds stress $\overline{u'v'}$ and $\overline{u'w'}$. Using Eq. (14), the leading terms of Eqs. (9) and (10) were calculated from the interpolated experimental data for a range of values of l_d and compared to the experimental stresses. It was found that a value $l_d = 0.58$ *ft* was sufficient to maintain the dominant character of the experimental stress distributions, and to preserve the characteristic magnitude of these stresses. This value corresponds to approximately 85% of the propeller diameter, 23% of the beam, and 71% of the draft. Since the inboard rotation tests did not include hot-film measurements, the same value of l_d was used in the simulation of those experiments. Dependent variables at computational points located outside of the measurement domain were smoothly blended to values consistent with the boundary conditions, freestream conditions at the bottom and right boundaries and symmetry conditions at the $Z = 0.0$ and $Y = 0.0$ planes. In the following section the results of the simulations are discussed.

4. RESULTS OF THE SIMULATIONS

TWAKE solves the governing equation system in a non-dimensionalized form wherein the independent variables are non-dimensionalized by a characteristic length and the independent variables are non-dimensionalized by the characteristic density and appropriate powers of the characteristic velocity. These were taken as the model ship beam, $B = 2.5$ *ft*, the ambient density, $\rho_0 = 1.035$ *lb**f*-*sec*²-*ft*⁻⁴, and the tow velocity, $U_0 = 6.76$ *ft*-*sec*⁻¹. The origin for the *X* axis was further offset by the distance from the AP to the initial computational plane, $X_0 = 10.0$ *ft* in both simulations. In the following sub-sections, for each of the simulations in turn, full planar numerical solutions (for the experimentally observed fluid properties) are presented at the computational planes corresponding to the measurement locations shown in Table 2.

Outboard Propeller Rotation

The first entries in each of Figs. 3 and 4 are contour plots of the non-dimensional, interpolated, experimental data at the $X = 10.0$ *ft* station for the streamwise mean velocity and the turbulence kinetic energy, respectively. The initial velocity distribution is characterized by a drag wake ($\bar{U}/U_0 < 1.0$) near the free surface and an overthrust

region ($\bar{U}/U_0 > 1.0$) in the vicinity of the propeller disk (projected aft). The overthrust fluid is bifurcated into distinct regions, each having local maximum velocities of approximately $0.08U_0$. The maximum velocity deficit in the drag wake, which also exhibits several local extrema, is $0.09U_0$. The initial kinetic energy distribution contains local maxima in the propeller disk and immediately at the free surface. The maximum magnitude corresponds to a characteristic velocity of turbulence exceeding $0.06U_0$. The initial distribution of the non-dimensional swirl velocity,

$$V_s \equiv \frac{1}{U_0}(\bar{V}^2 + \bar{W}^2)^{1/2},$$

is shown in Fig. 5a. There are two distinct vortical structures present which are approximately coincident with the two overthrust lobes. Whereas the overthrust is about the same in both lobes the two structures are quite different. The uppermost and strongest is evidently due to the propeller and the swirl magnitude approaches $0.10U_0$. The lower counter-rotating vortex presumably was shed from the hull or the control surfaces. The fluid in the propeller swirl is considerably more turbulent than that in the lower vortex (Fig. 4a). At the depth $Z/B \approx -0.4$, the two vortices are mutually acting to drive fluid toward the ship centerline. This action is assumed to be the cause of the bifurcation shown in Fig. 3a. Figure 6a is the initial distribution of the resultant of the two principal Reynolds stresses,

$$\tau_z \equiv \frac{1}{U_0^2}((\overline{u'v'})^2 + (\overline{u'w'})^2)^{1/2}.$$

In this case the displayed data are not the actual (interpolated) measurements but rather are derived from Eqs. (9-10) and (14) using the experimental mean velocity and turbulence fields. The measured characteristic level of shear has been preserved through the choice of the dissipation length scale. The computed stress is predominantly radial in the overthrust fluid and has a dominant vertical component in the drag wake.

Figures 3b through 3d are contour plots of the computed mean streamwise velocity at each of the three downstream measurement planes located 16.0, 22.0, and 30.0 ft aft of the model, respectively. The contours near the free surface (drag region) show that by $X = 30.0$ ft the several local extrema in the velocity have diffused to a single extremum near $Y/B = 0.3$. As the solution proceeds downstream the minimum velocity, or maximum drag velocity at the surface, moves to outboard, existing finally at $Y/B = 0.4$. The overthrust portion of the velocity distribution in the subsurface wake essentially maintains the bifurcated structure characteristic of the initial condition. The maximum velocity peaks are convected inboard by the propeller swirl and finally exist near the model centerline. The computation shows that by $X = 30.0$ ft, overthrust fluid ($\bar{U}/U_0 > 1.0$) has been carried to the free surface by the secondary flow. At this downstream plane the maximum subsurface overthrust is approximately $0.04U_0$, while the maximum at the surface is $0.02U_0$. The profiles of the evolving turbulence kinetic energy (Figs. 4b-4d) also exhibit the convective action of the swirl flow. As the solution proceeds downstream the maximum values of turbulence energy exist at the free surface near $Y/B = 0.2$.

The downstream decay of the swirl velocity distribution is observed in Figs. 5b through 5d. At $X = 30.0$ ft the swirl has decayed to about one-third of the initial

level. The lower inboard rotating vortex, initially existing in fluid of considerably less turbulence than the upper, decays at a relatively slower rate such that by $X = 30.0 \text{ ft}$ the two vortices are of comparable strength. The evolving shear stress distributions shown in Figs. 6b through 6d show that by the final measurement station, the stress is predominantly horizontal near the free surface. The shear, of course, corresponds directly with the velocity gradient field apparent from the contour spacing of Figs. 3a through 3d.

Figures 7a and 7b are contour plots of the streamwise velocity and turbulence kinetic energy, respectively, in the plane of the mean free surface ($Z/B = 0.0$). In these figures the port-side of the wake ($Y/B < 0.0$) has been depicted by symmetric reflection of the computed starboard-side solution. The frame of reference for the velocity has been transformed to a stationary one such that negative contour values depict fluid moving in the direction of ship motion (left in Fig. 7a) and positive contour levels denote overthrust fluid moving in the opposite direction. The contours show that the three velocity minima on each side of the wake merge to a single minimum by $(X - X_0)/B \approx 2.0$ ($X/B = 15.0 \text{ ft}$) and that this minimum slowly moves away from the ship centerline. The minimum velocity (maximum drag velocity) at the end of the computational domain is about 4% of the tow velocity. Overthrust fluid from the propeller thrust begins to reach the surface at $(X - X_0)/B = 5.0$, which corresponds to nearly 18.0 ft aft of the model. As the wake turbulence decays in the downstream direction (Fig. 7b), the peak values in the surface plane move toward the ship centerline. The characteristic magnitude of the fluctuating turbulence velocity defined as $K^{0.5}$ is approximately $0.04U_0$ at the end of the computation. This is of the same order as the maximum mean velocity in the drag wake.

Figures 8a and 8b are plots of the longitudinal decay of certain characteristic values of the streamwise velocity deficit (or excess) and turbulence kinetic energy, respectively. The curves labeled "maximum" refer to the variation of the maximum value of the variable anywhere in the cross-plane ($X/B = \text{const.}$) whereas those labeled "maximum in surface plane" refer to the variation of the maximum value of the variable in the surface plane ($Z/B = 0.0$) only. For the velocity the variation of the minimum (maximum deficit) is also shown. While the curves are generally self-explanatory, Fig. 8b deserves some comment. This figure and Fig. 4a show that essentially identical local maxima in the kinetic energy exist in both the surface plane and the subsurface region. However, after a developmental region, the turbulence in the surface plane decays at a faster rate. Still further along in the developing wake the trend reverses and the subsurface turbulence decays at a faster rate. Finally at the end of the computation the maximum turbulence is at the free surface. This behavior can be explained with recourse to several of the preceding figures. Figures 3a and 6a show that in the initial plane the larger values of the Reynolds stresses and the velocity gradients exist in the subsurface region. The production term in Eq. (12) is therefore higher in this region. The dissipation resembles the kinetic energy (Fig. 4a) through Eq. (14) and is of comparable magnitude in both regions. Thus the balance is such that the turbulence at the surface will decay faster in the upstream part of the wake. As the wake develops (Figs. 3c and 6c) the production of turbulence becomes comparable in both regions and thereafter convection plays an increasingly important role transporting turbulent fluid to the surface. The onset of surface renewal with fluid from below is apparent in Fig. 8a near $(X - X_0)/B = 5.0$.

Inboard Propeller Rotation

The initial conditions for the simulation of the inboard rotation experiment are shown as the first entries in each of Figs. 9 through 12. Although the Froude and Reynolds numbers are identical for the inboard and outboard rotation experiments, the measured fluid properties are significantly different at the initial $X = 10.0$ ft axial plane. Figure 9a shows that the velocity varies from $0.87U_0$ in the drag region to $1.11U_0$ in the propeller thrust. These extrema are significantly different than the limiting values of $0.91U_0$ and $1.08U_0$ observed in the outboard rotation experiment. Also of note in this figure is the presence of a single velocity peak in the thrust fluid located relatively more to the outboard, rather than the more inboard and bifurcated structure manifest in the first experiment. Near the free surface at the model centerline there is a small region of excess velocity ($\bar{U}/U_0 \approx 1.02$). Although this small velocity excess may be comparable to the experimental error, the qualitative structure of the isovels in this area suggests a distinctly weakened or even non-existent drag wake along the ship centerline. The initial distribution of turbulence kinetic energy (Fig. 10a) shows maximum levels 50% greater than in the outboard experiment. In this case the fluid near the free surface is considerably less turbulent than that in the propeller swirl. The initial propeller swirl (Fig. 11a) is considerably less, only about $0.063U_0$, and located more to outboard which is consistent with the velocity profile in Fig. 9a. The higher thrust velocity and lower swirl suggests more efficient propeller operation in this experiment. The lower vortex apparent in the outboard data is absent. There is a significant outboard rotating vortex near the free surface. This vortex, possibly induced by the propeller swirl, may be responsible for transporting overthrust fluid to the surface and producing the weakened drag wake noted in the discussion of Fig. 9a. The initial Reynolds stress distribution is shown in Fig. 12a and is characterized by predominantly radial shear in the thrust fluid. The magnitude is a factor of two higher than in the first experiments due to the higher turbulence kinetic energy and mean velocity gradients.

Table 2 shows that data was collected during the inboard rotation tests at two additional downstream planes, $X = 16.0$ ft and $X = 30.0$ ft. Although these particular tests were made while towing the model at 6.0 knots rather than at the speed of 4.0 knots used in the measurements at $X = 10.0$ ft, it may be possible to compare the results of the simulation to this data in a qualitative manner. The second and third entries in each of Figures 9 through 12 are the computed results for the selected fluid variables at the two downstream stations.

Figures 9b and 9c show that as the wake evolves to $X = 30.0$ ft the surface drag velocity decreases to about $0.03U_0$ while the maximum propeller overthrust has decreased to $0.04U_0$. By the final station the drag wake has been diffused and advected into the center of the wake. The maximum level of turbulence kinetic energy (Fig. 10c) has decayed to approximately one-third the magnitude that existed in the initial plane. The maximum turbulence levels remain well below the plane of the mean free surface. In contrast to the outboard simulation, there is no obvious effect on either the mean velocity or turbulent energy due to convection by the swirl flow. The swirl, shown in Figs. 11b and 11c, decays to 20% of the initial level by $X = 30.0$ ft. The computed Reynolds stress distributions for the downstream planes are shown in Figs. 12b and 12c. The dominant horizontal component of shear stress which was present in the outboard experiments is absent by $X = 30.0$ ft.

Figures 13a and 13b are contours plots of the streamwise velocity deficit and the turbulence kinetic energy in the plane of the mean free surface. These distributions strongly resemble their outboard simulation counterparts (Fig. 7) discussed in the previous section. The small velocity excess mentioned in connection with Fig. 9a has vanished by $(X - X_0)/B = 1.0$. Also worthy of note in Fig. 13a is the significantly smaller horizontal strain ($\partial \bar{U}/\partial Y$) than that evident in Fig. 7a.

Figures 14a and 14b are plots of the longitudinal variation of characteristic values of the velocity and turbulence kinetic energy and illustrate portions of previously described results in a different form.

5. COMPARISON AND FINAL REMARKS

Figures 15a and 15b are included to provide a means of comparison between the two simulations discussed above. These calculations, performed subsequent to the original computations, also extended the solution considerably further downstream as shown in the figures. It should be noted that these solutions began to encounter the freestream boundaries in the transverse plane at approximately $(X - X_0)/B = 50.0$ and, consequently, the results beyond that region do not reflect the actual physical background environment. Until that point, however, all variables appear to have achieved a power law decay with respect to the streamwise coordinate as shown in the figures. Keeping in mind that these flow fields are considerably more complex than any of the "classical" flows, the indicated asymptotic behavior seems reasonable. The major contrasts between the two simulations are that the inboard rotation velocities decay at a faster rate than their outboard rotation counterparts. Consistent with that trend, the inboard rotation turbulence decays more slowly resulting in a correspondingly higher turbulent diffusivity over the computational domain. The ultimate decay is influenced by the initial dissipation distribution as well as the constants of the model. In the absence of data for the shear stress, the dissipation for the inboard simulation was obtained by requiring the same value of the length scale that was used in the outboard simulation. The local turbulence time scale, proportional to K/ϵ , is then computed to be different for the two flows.

A final observation to be made from Fig. 15b regarding the inboard rotation simulation is that the maximum level of turbulence kinetic energy do indeed exist at the free surface after $(X - X_0)/B \approx 20.0$, a characteristic that was observed for the outboard rotation computation (Fig. 8b).

In summary, the principal characteristics of the computed flow fields are that:

- 1) In the outboard simulation, the propeller thrust is bifurcated into two distinct regions which migrate toward the centerline of the wake and, by symmetry, merge with those formed by the port propeller. The upper of the overthrust regions eventually is convected to the free surface by the secondary flow and this acts to displace the original free surface drag wake to the outboard. This evolution combined with the eventual arrival of maximum turbulence kinetic energy levels at the surface results in relatively high transverse strain rate and Reynolds shear stress.
- 2) In the inboard simulation, the propeller thrust wake remains unimodal and essentially maintains spatial stationarity. Initial and small levels of velocity excess at the surface near the wake centerline quickly dissipate as the port and starboard

drag wakes merge into a single diffuse velocity deficit region. This results in considerably smaller transverse strain than in the outboard rotation simulation. The significantly higher levels of turbulence kinetic energy produce correspondingly greater values for the turbulent diffusivity and therefore faster decay rates for the fluid properties.

The computed differences in results for the two cases are significant and stem from differences in the initial plane data together with the assumption of equal dissipation scales for the two situations. In lieu of further guidance from detailed experiments, the latter assumption appears appropriate. It is fascinating that the differences seen in the two measured data sets may be attributed solely to the change in direction of propeller rotation. Undoubtedly, further experimentation will be needed to fully explore these changes in a complex flow field. It is highly recommended that these experiments include provisions for flow visualization of the major flow features and of the surface flow patterns which clearly are sensitive to the initial wake structure.

6. ACKNOWLEDGMENTS

Funds for this work were jointly provided by the Office of Naval Research (Code 12) and the Office of Naval Technology (Code 21) Surface Ship Wake Reduction Program (technically managed by DTNSRDC).

7. REFERENCES

- [1] D. J. Fry and Y. H. Kim. "Bow Flow Field of Surface Ships." Proc. Fifteenth Symposium Naval Hydrodynamics. 1985.
- [2] W. T. Lindenmuth, private communication: data from the model experiments at DTNSRDC - outboard propeller rotation, Aug. 1986.
- [3] W. T. Lindenmuth, private communication: data from the model experiments at DTNSRDC - inboard propeller rotation, Jan. 1987.
- [4] A. J. Baker, *Finite Element Computational Fluid Mechanics*. McGraw-Hill, Hemisphere, New York, 1983.
- [5] A. L. Cooper, "Turbulent Wake of a Submerged Flat Plate." NRL Memorandum Report 5521, April, 1985.

Table 1. Model Ship Parameters

Model	High Speed Surface Ship
DTNSRDC No.	5415-1
Length*	18.8 <i>ft</i>
Beam	29.9 <i>in</i>
Draft	9.8 <i>in</i>
Prop Dia.	8.16 <i>in</i>
Block Coef.	0.506
Tow Speed	4.0 <i>knots</i>
Froude No.	0.28

* (length between forward and aft perpendiculars)

Table 2. Points/data planes from LDV and HF anemometry

<i>Feet from AP</i>	-1.7		-1.1		-0.4		6.1		10.0		16.0		22.0		30.0	
Speed, <i>knots</i>	4	6	4	6	4	6	4	6	4	6	4	6	4	6	4	6
Outboard, LDV		96		128		111			175*	138	280*†	279†	260*			167
Outboard, LDV												151				
Outboard, HF							70		73*		86*	68	75*		61*	
Inboard, LDV									175*			148				160
No Prop, LDV				117					130			182†				

* (forwarded to NRL)

†(denotes plane where symmetry about vertical plane was tested)

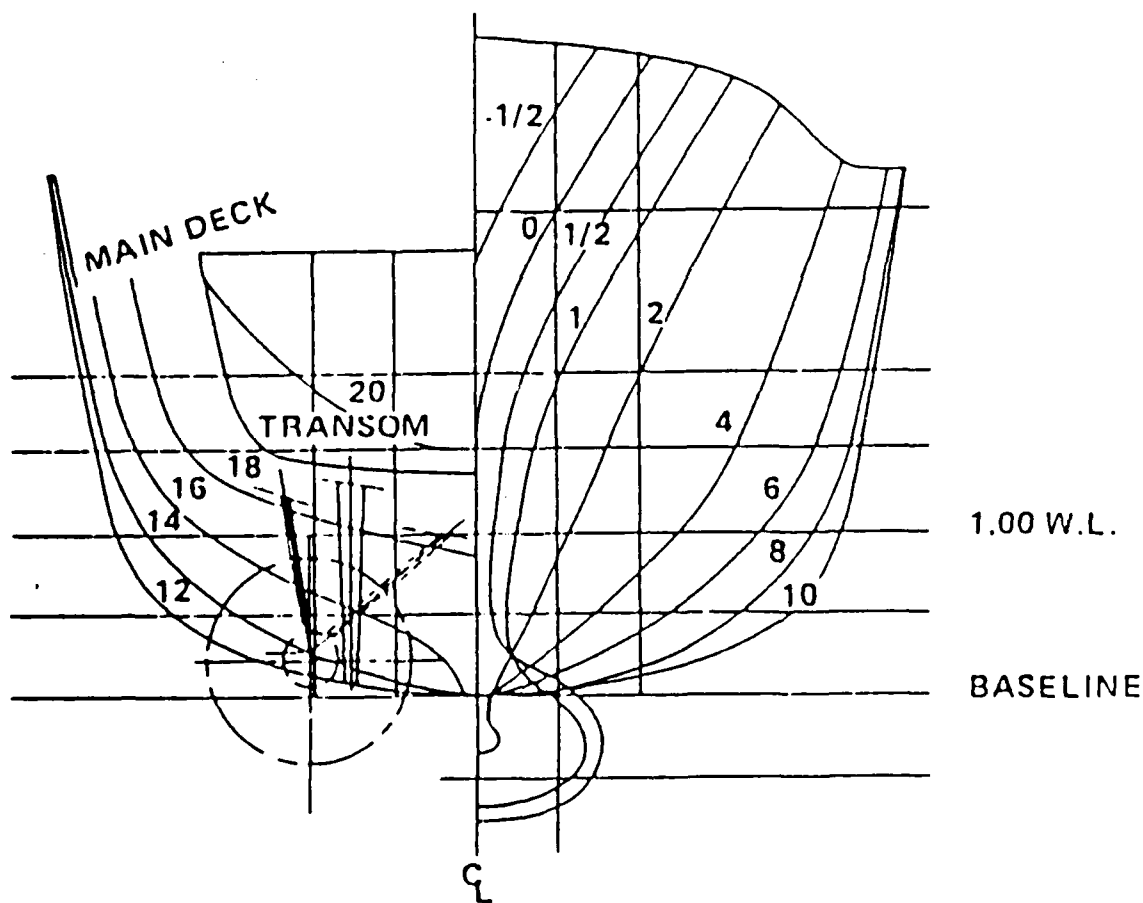
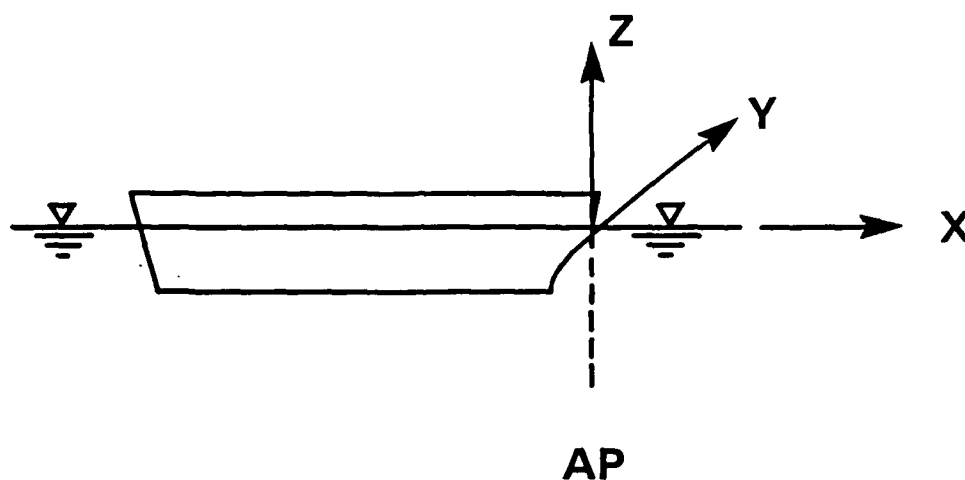
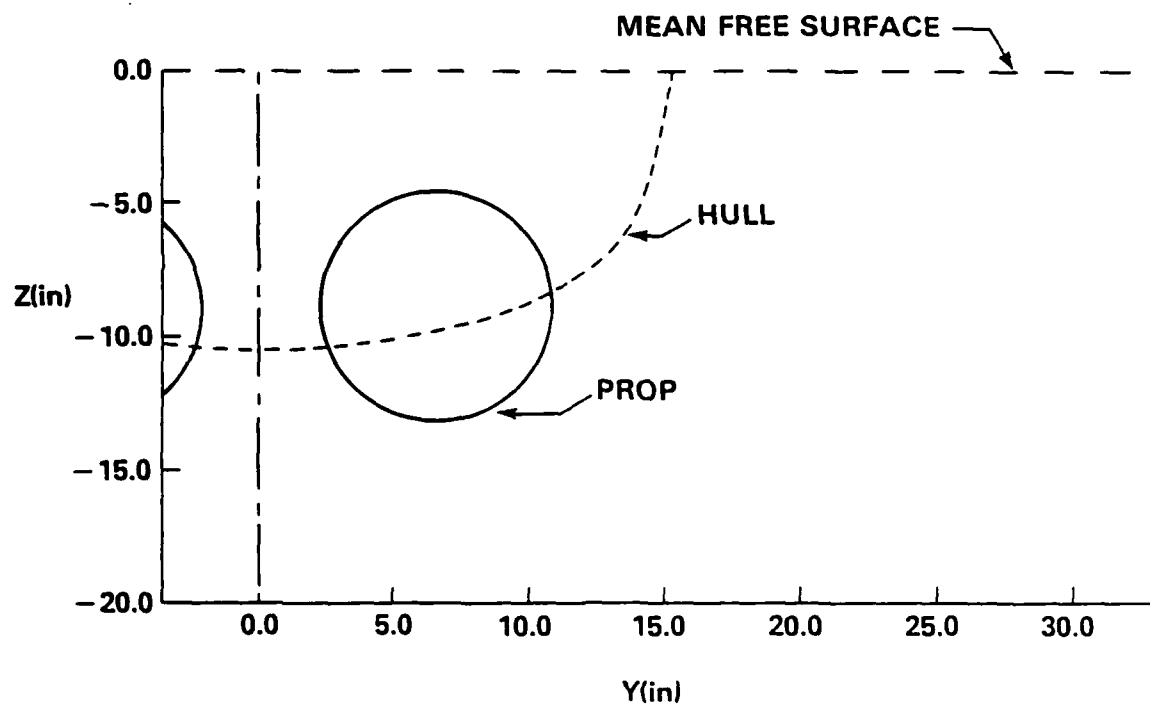


Fig. 1 - Body plan for high speed ship

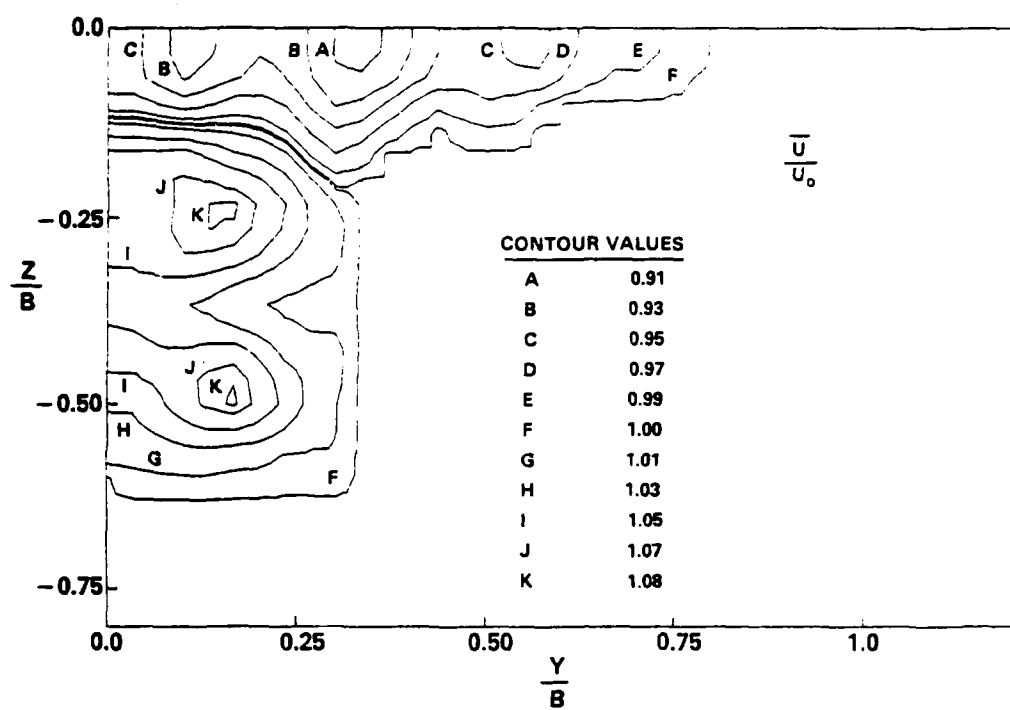


(a) model coordinate system

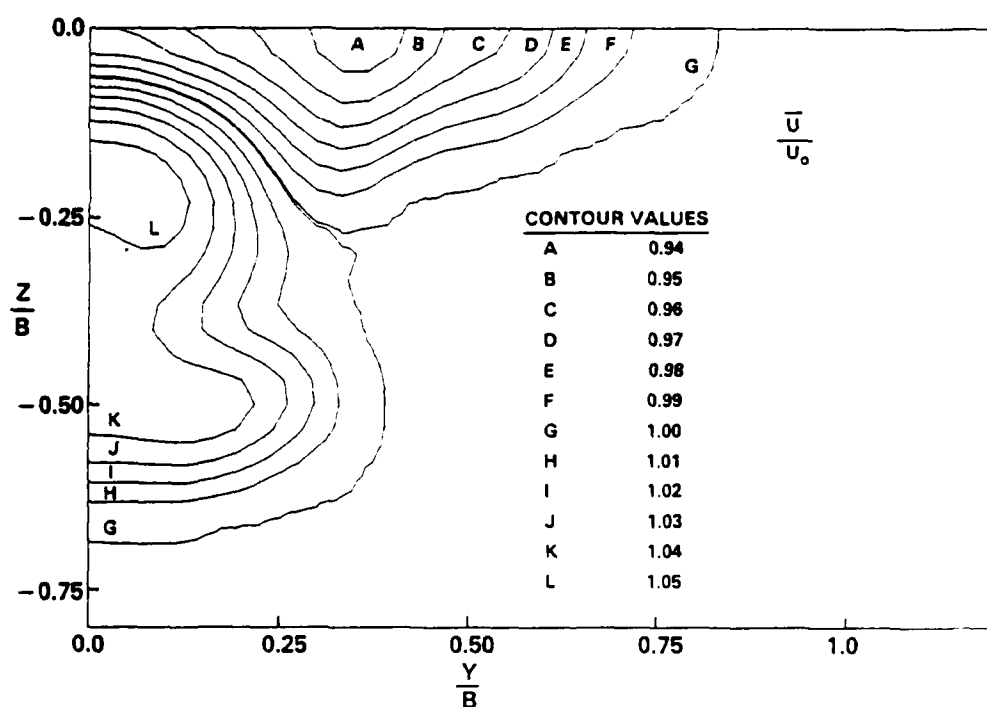


(b) typical measurement domain

Fig. 2 - Schematics of model coordinate system and transverse plane measurement domain

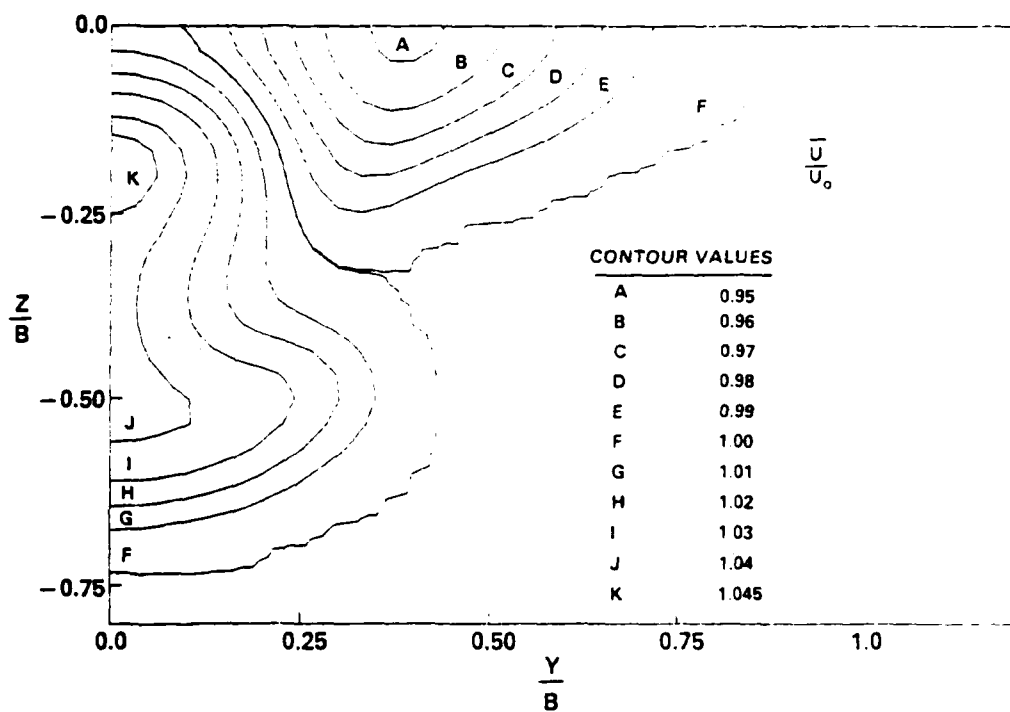


(a) $X = 10.0 \text{ ft}$

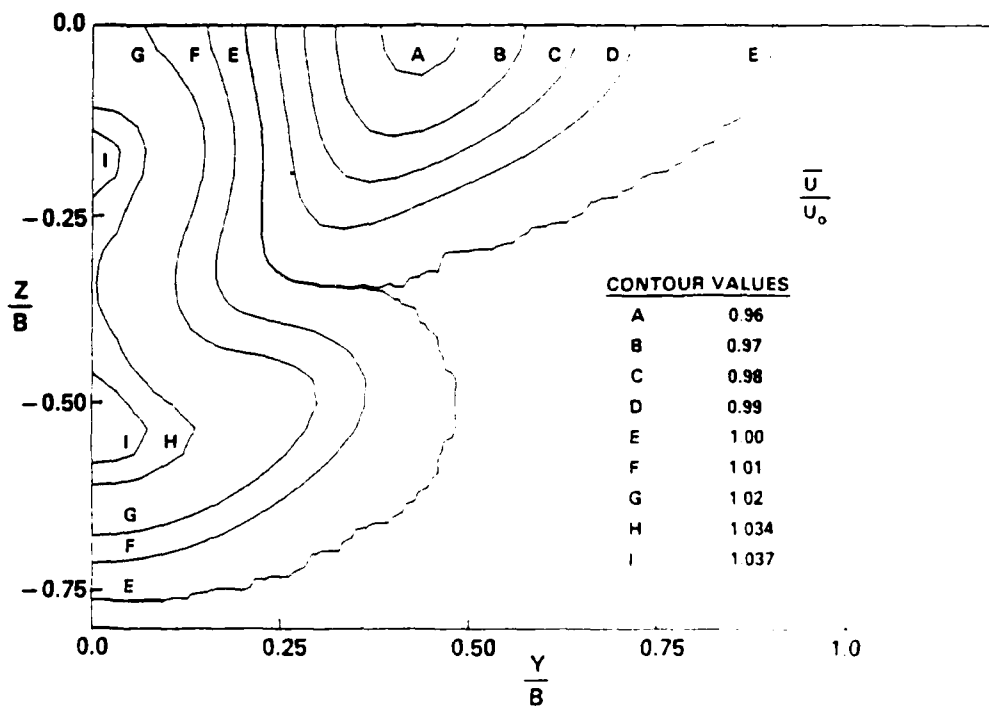


(b) $X = 16.0 \text{ ft}$

Fig. 3 - Contours of mean streamwise velocity: outboard rotation

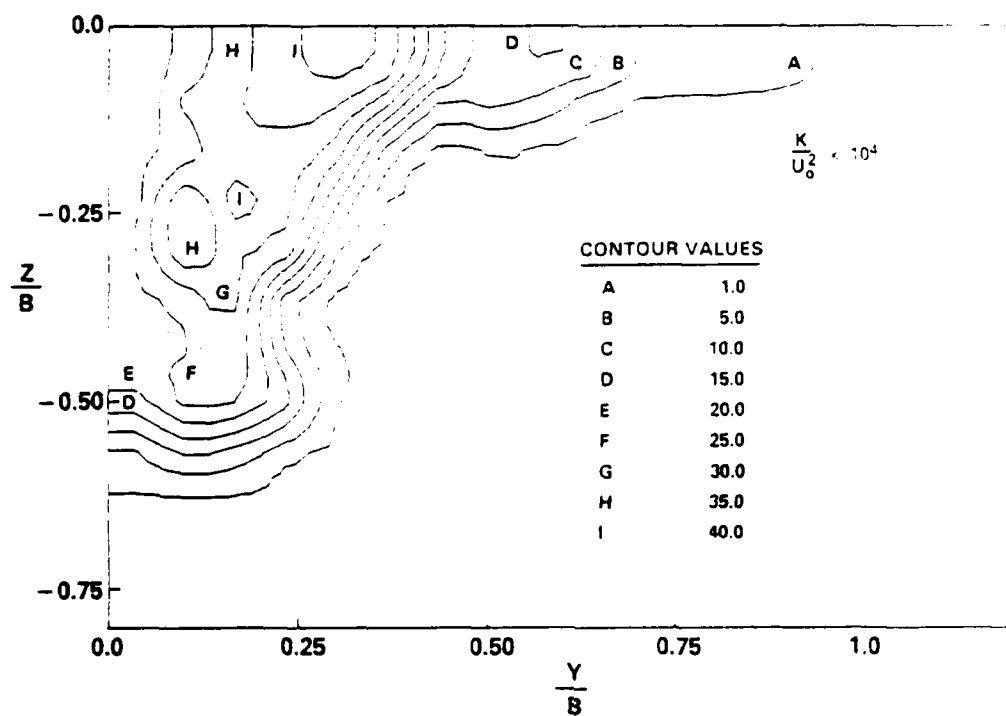


(c) $X = 22.0 \text{ ft}$

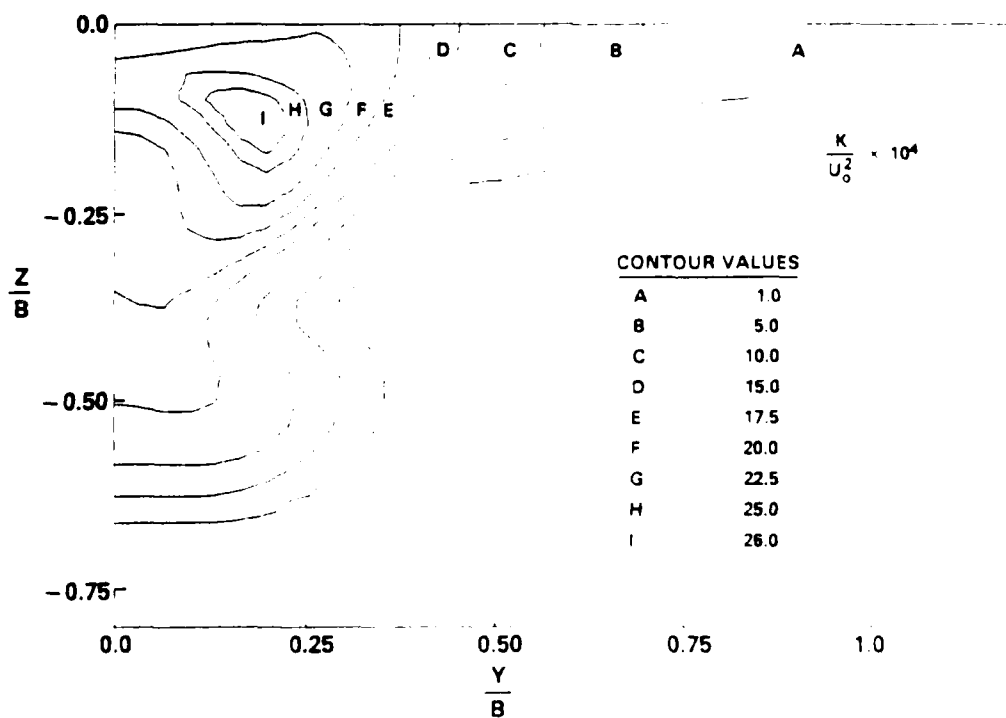


(d) $X = 30.0 \text{ ft}$

Fig. 3 (Cont'd) — Contours of mean streamwise velocity: outboard rotation

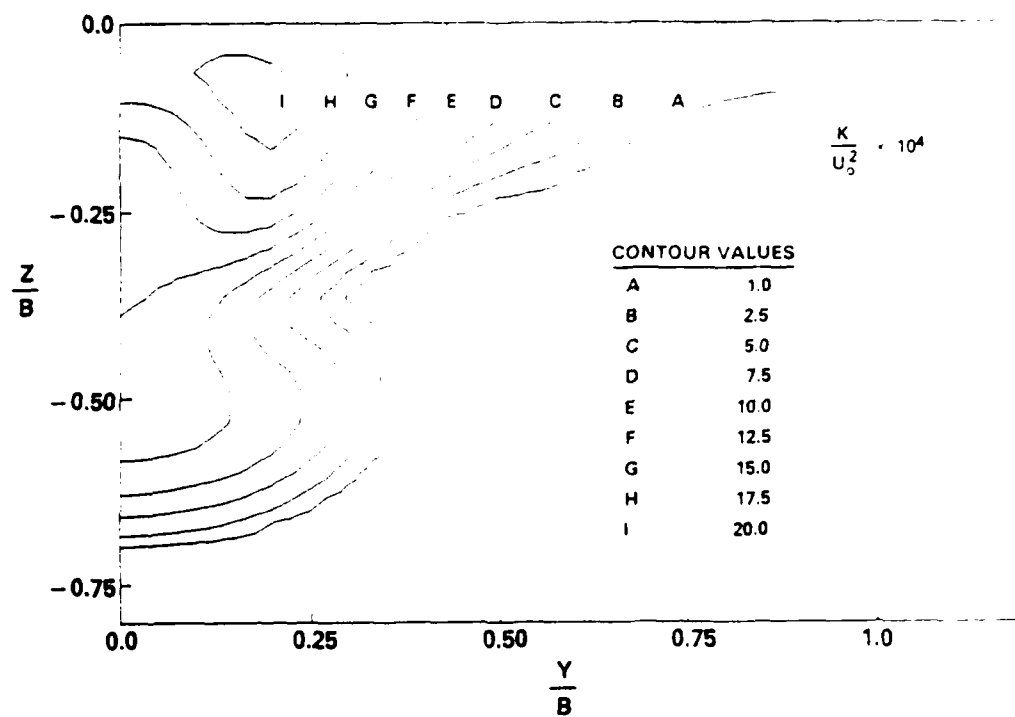


(a) $X = 10.0$ ft

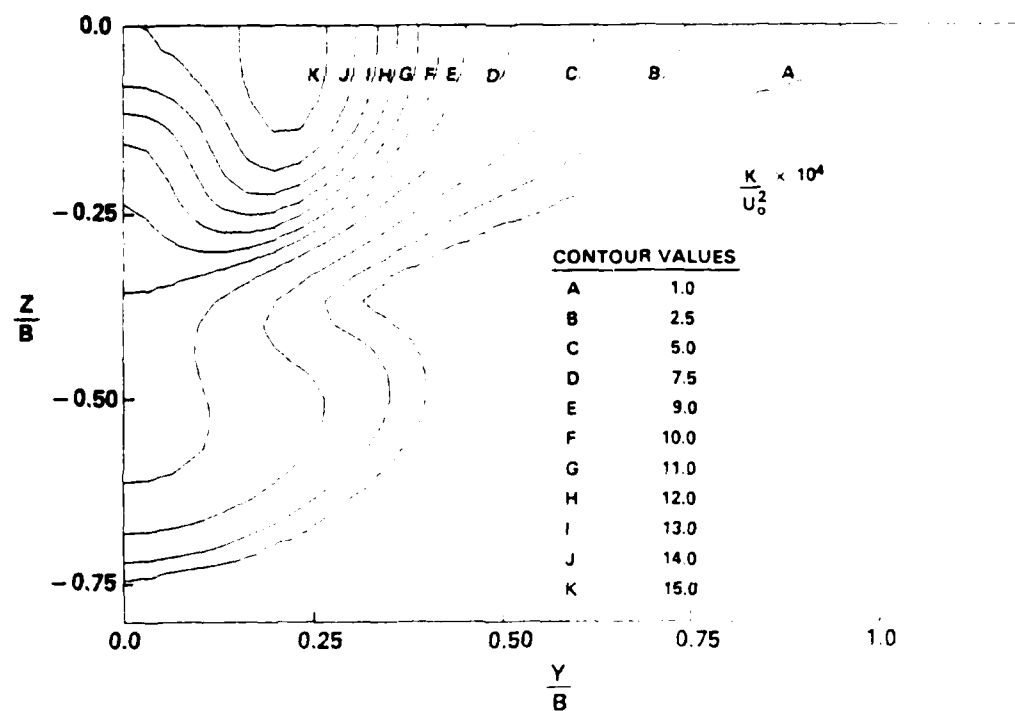


(b) $X = 10.0$ ft

Fig. 4 - Contours of turbulence kinetic energy, outboard rotation

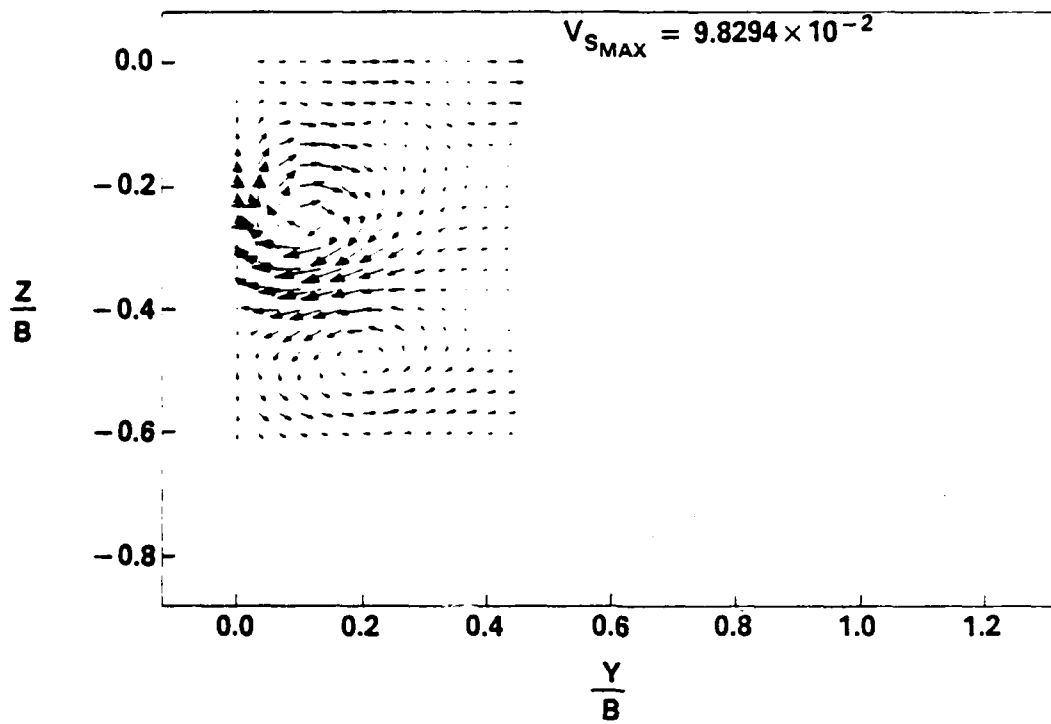


(c) $X = 22.0$ ft

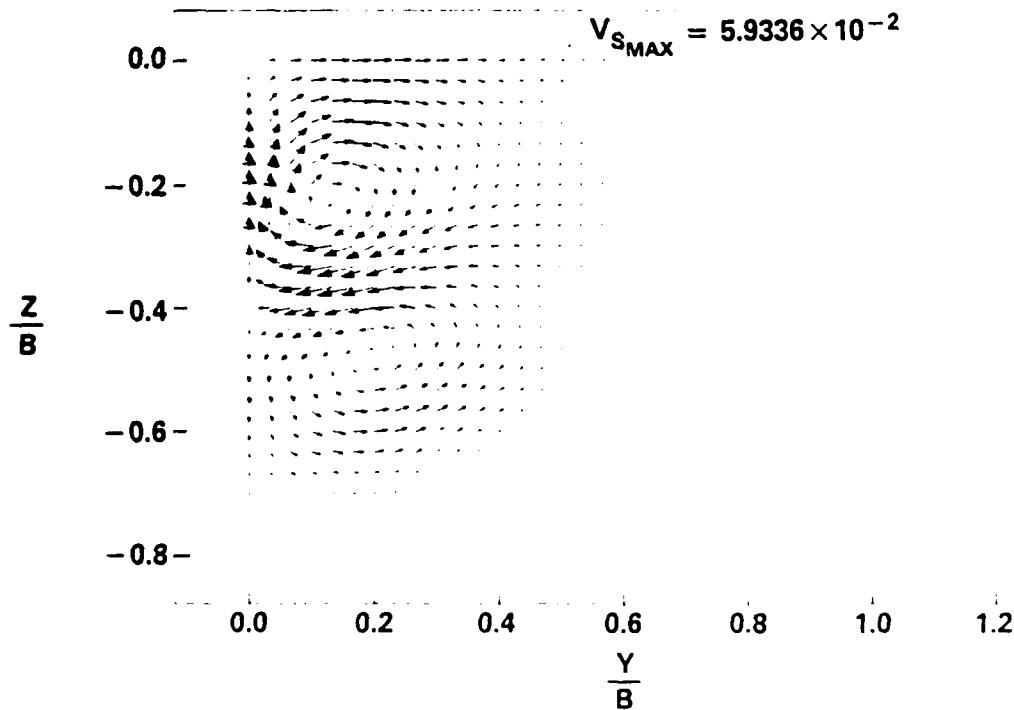


(d) $X = 30.0$ ft

Fig. 4 (Cont'd) — Contours of turbulence kinetic energy: outboard rotation

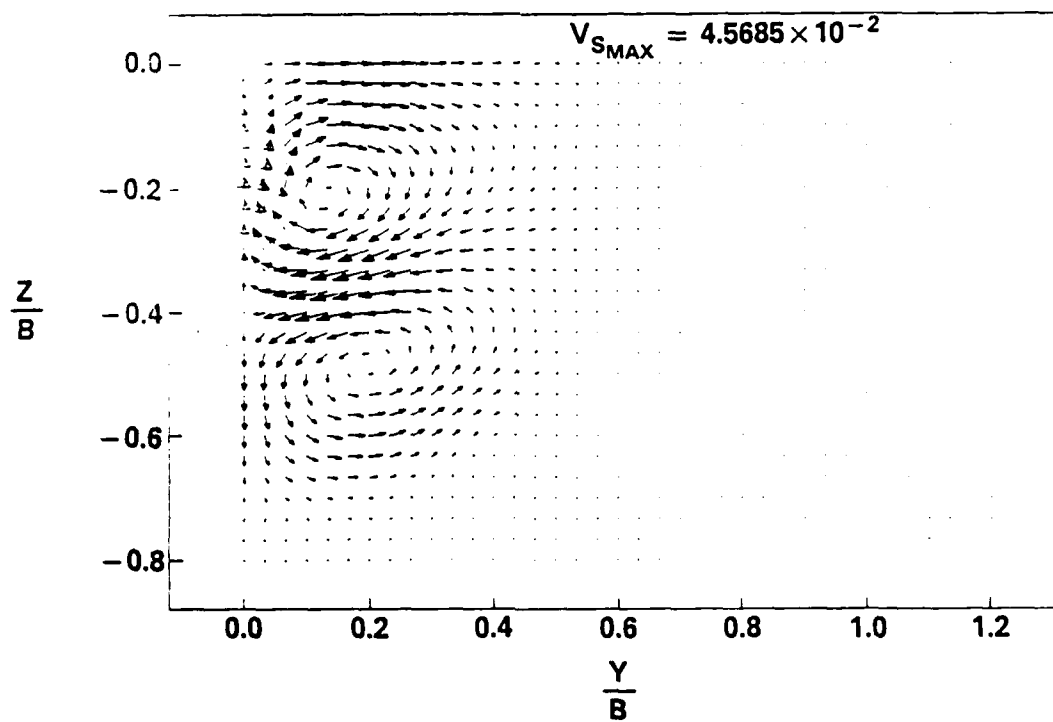


(a) $X = 10.0 \text{ ft}$

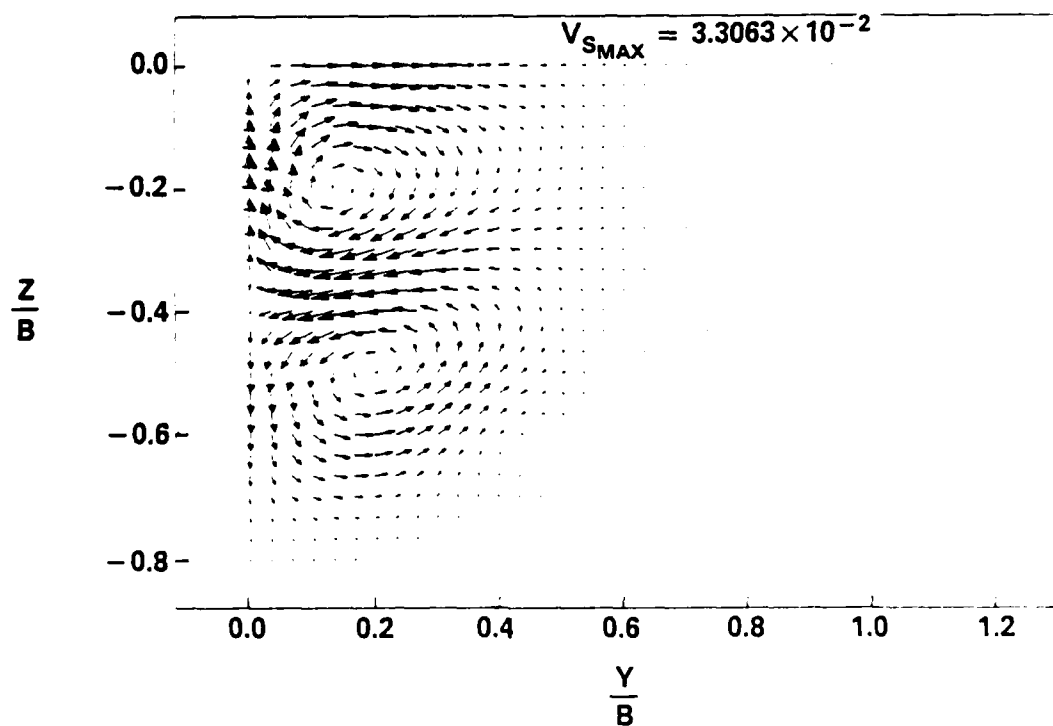


(b) $X = 16.0 \text{ ft}$

Fig. 5 - Swirl velocity vectors: outboard rotation

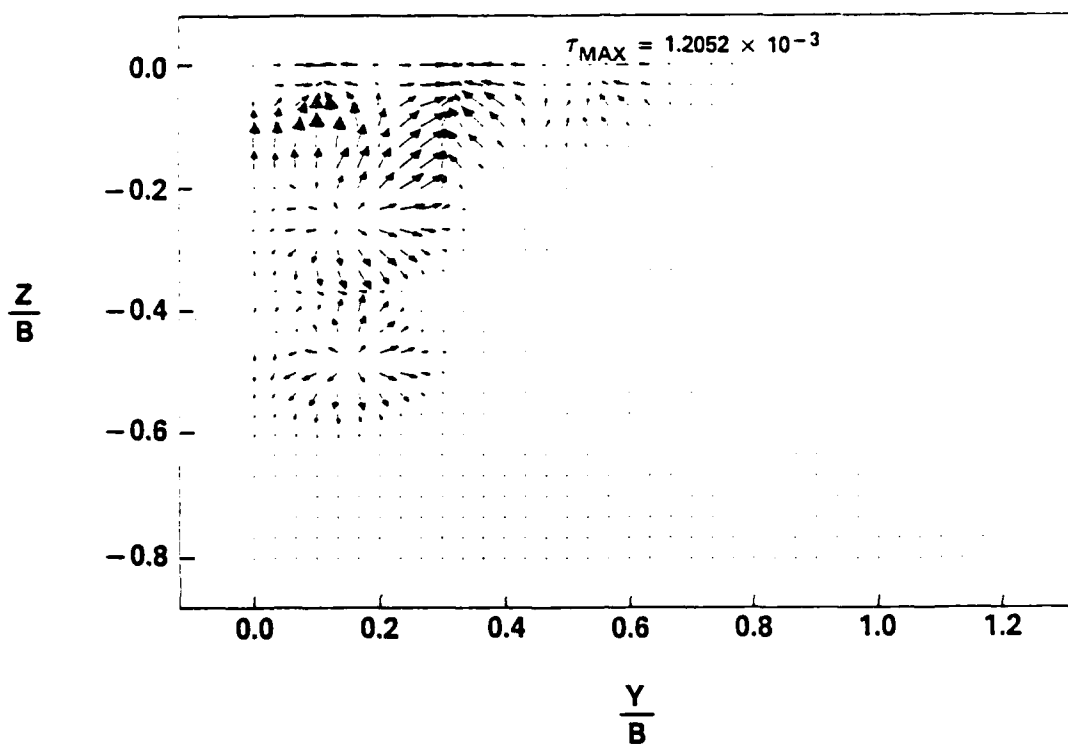


(c) $X = 22.0$ ft

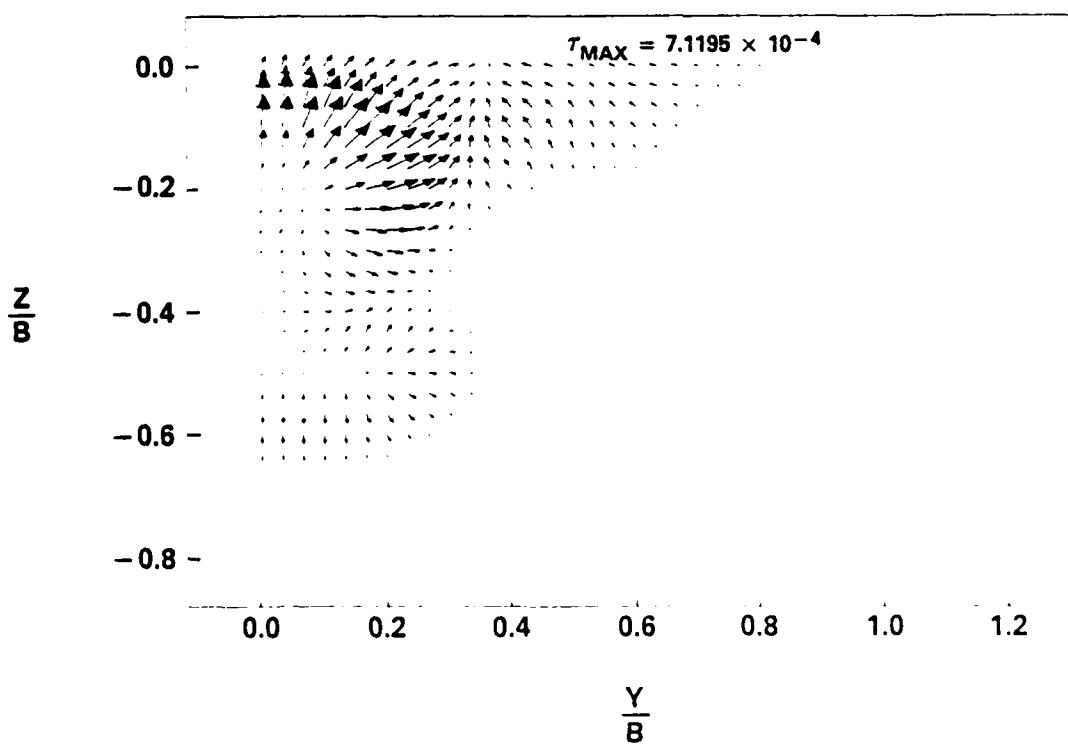


(d) $X = 30.0$ ft

Fig. 5 (Cont'd) — Swirl velocity vectors: outboard rotation

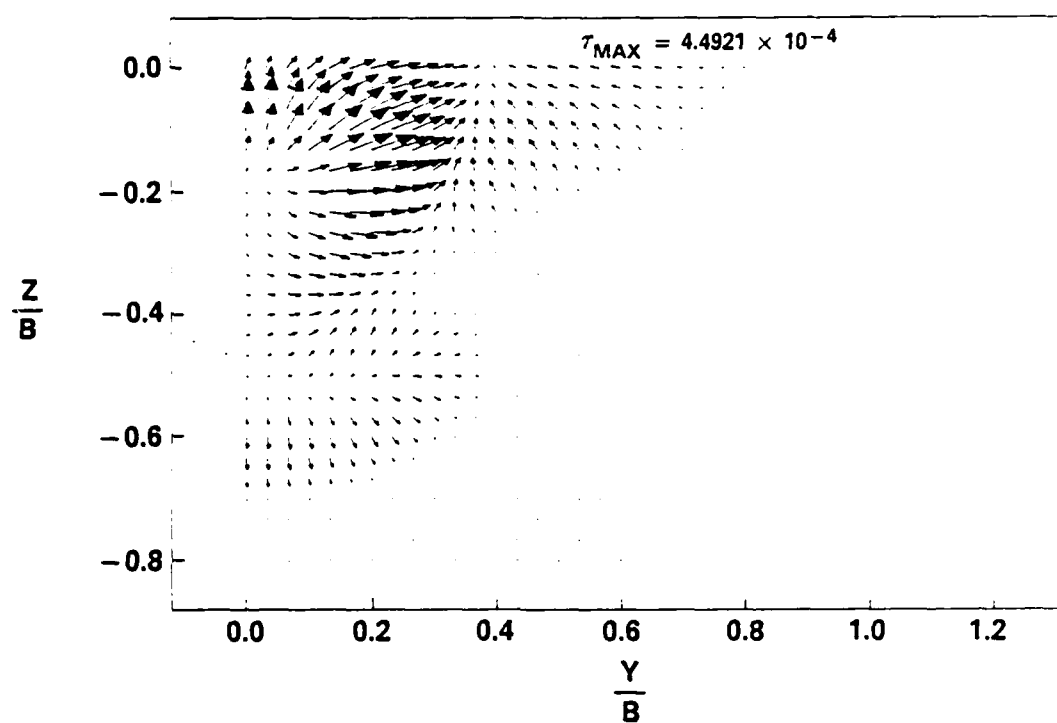


(a) $X = 10.0 \text{ ft}$

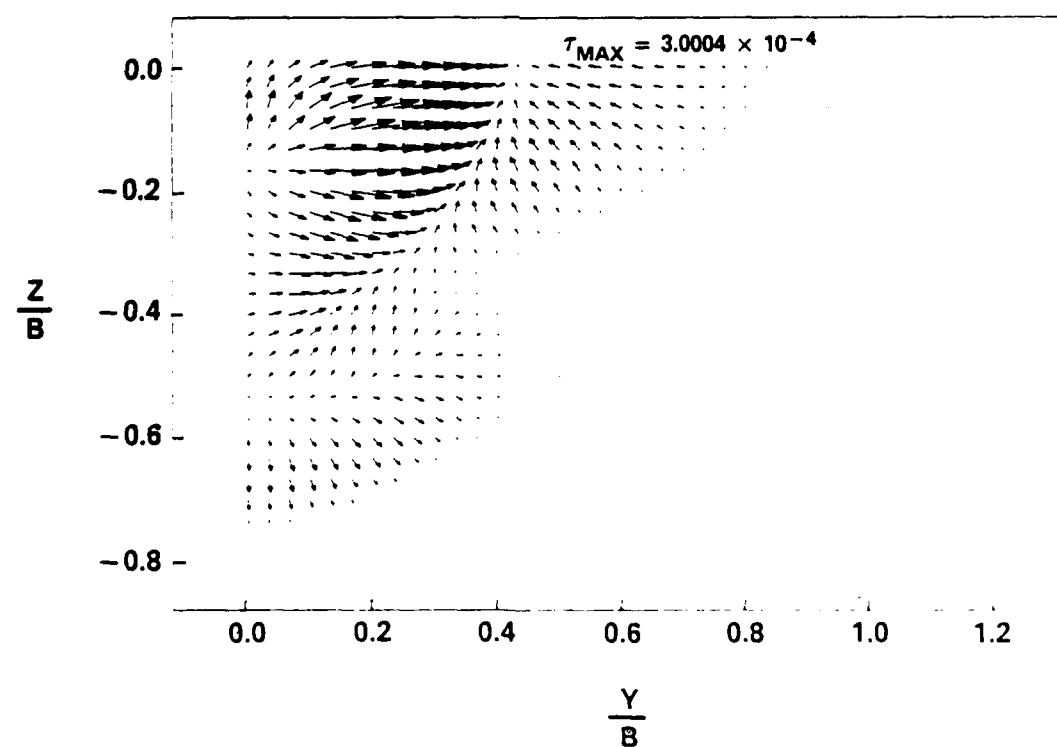


(b) $X = 16.0 \text{ ft}$

Fig. 6 - Reynolds stress distribution: outboard rotation

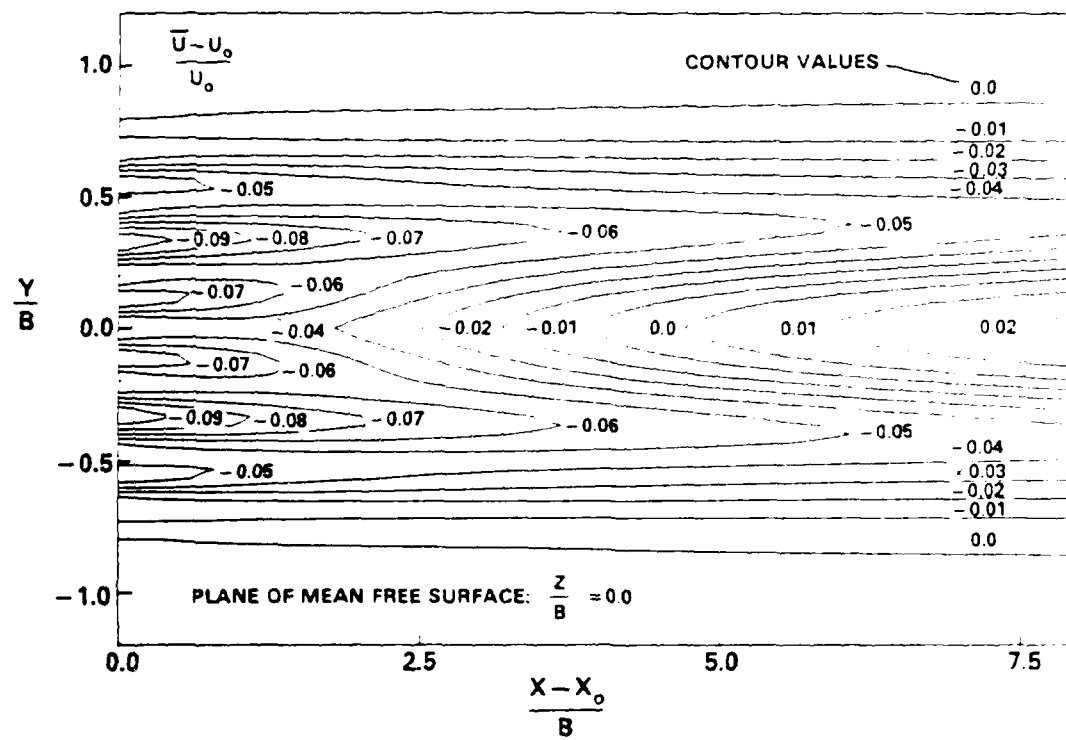


(c) $X = 22.0 \text{ ft}$

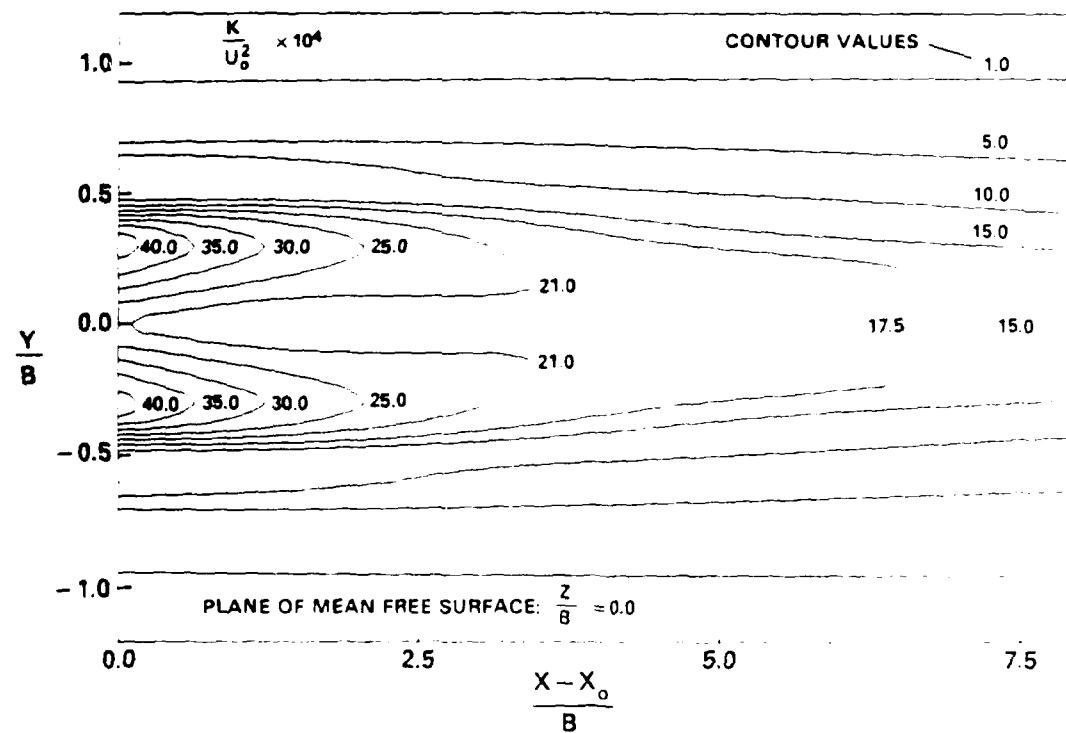


(d) $X = 30.0 \text{ ft}$

Fig. 6 (Cont'd) — Reynolds stress distribution: outboard rotation

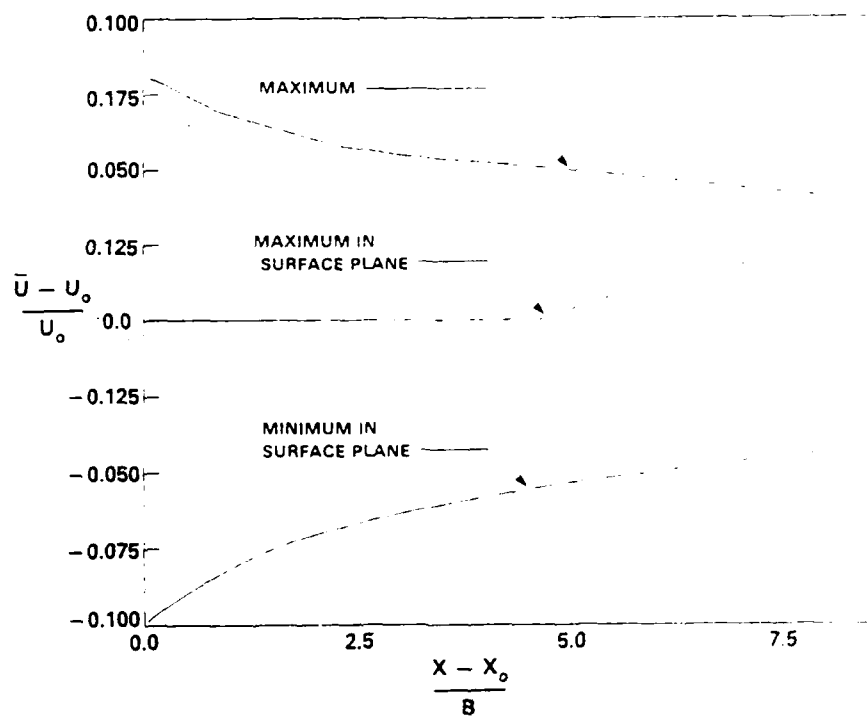


(a) streamwise velocity

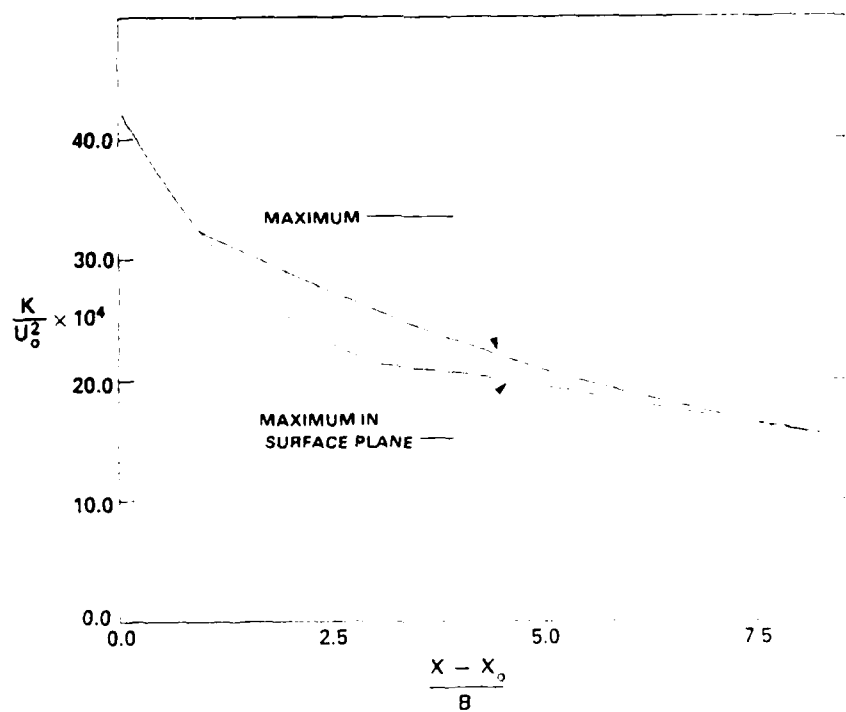


(b) turbulence kinetic energy

Fig. 7 - Contours of streamwise velocity and turbulence kinetic energy in plane of free surface: outboard rotation

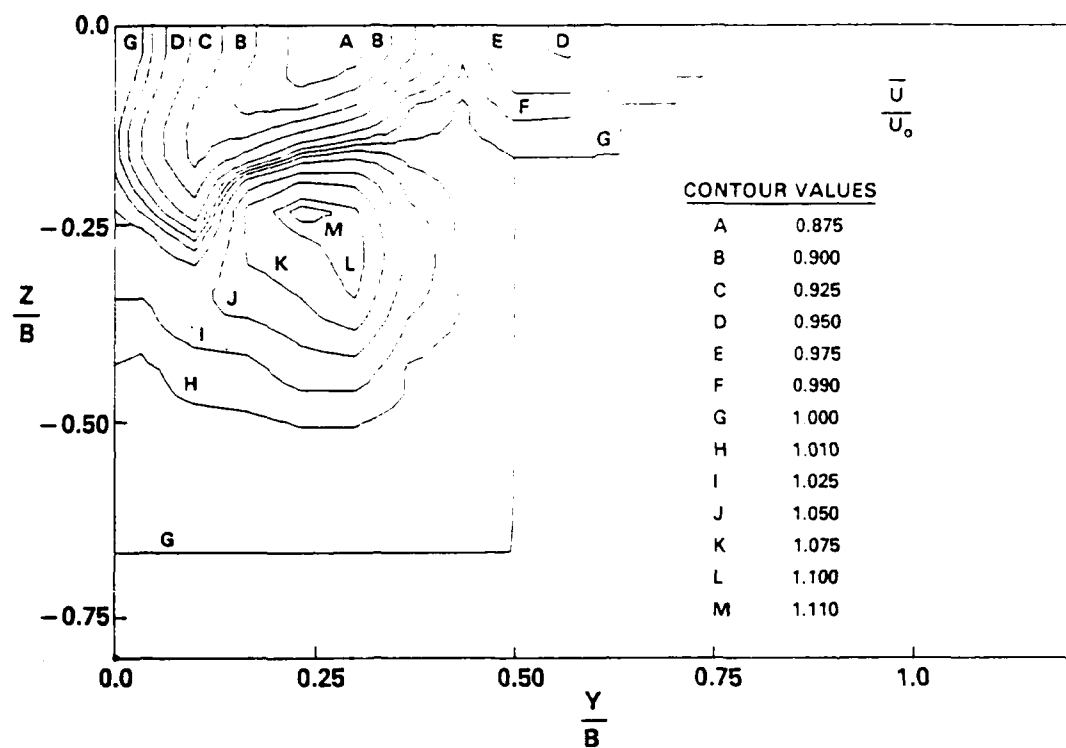


(a) streamwise velocity

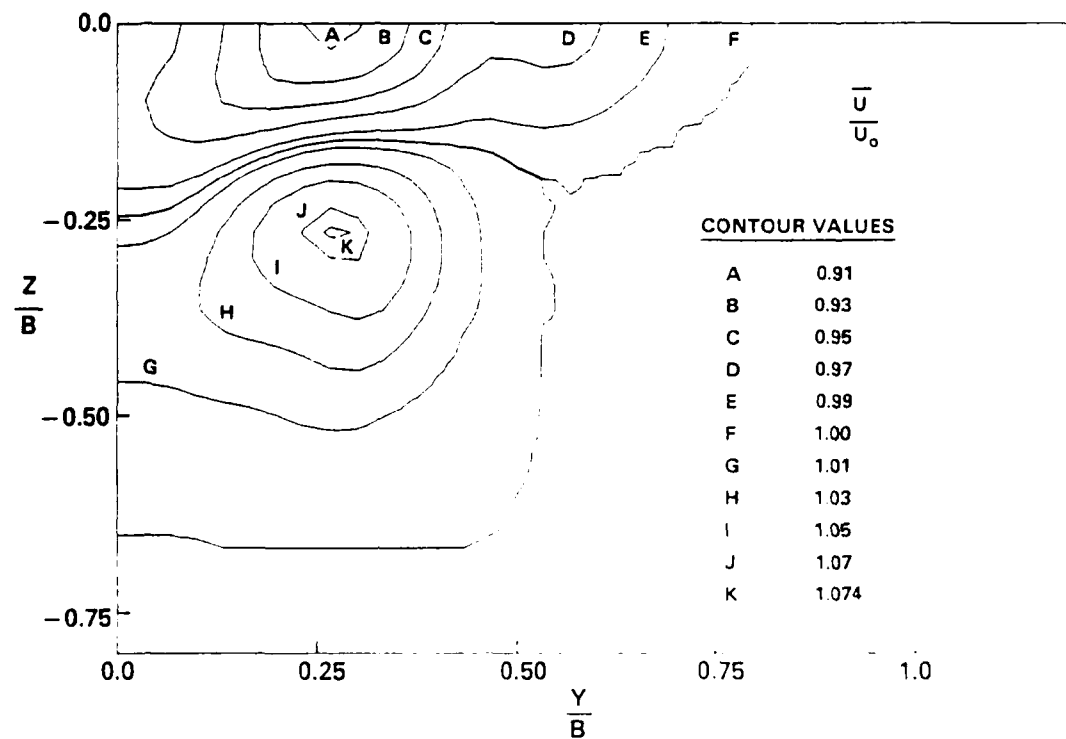


(b) turbulence kinetic energy

Fig. 8 - Axial decay of characteristic values of streamwise velocity and turbulence kinetic energy: outboard rotation

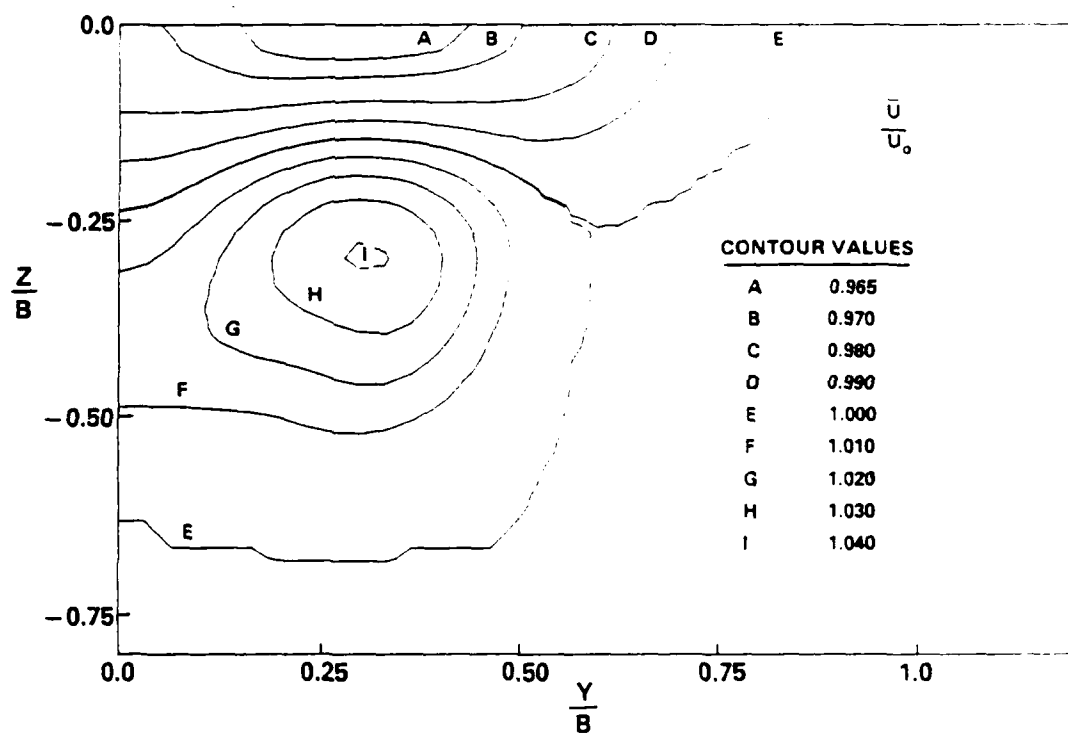


(a) $X = 10.0 \text{ ft}$



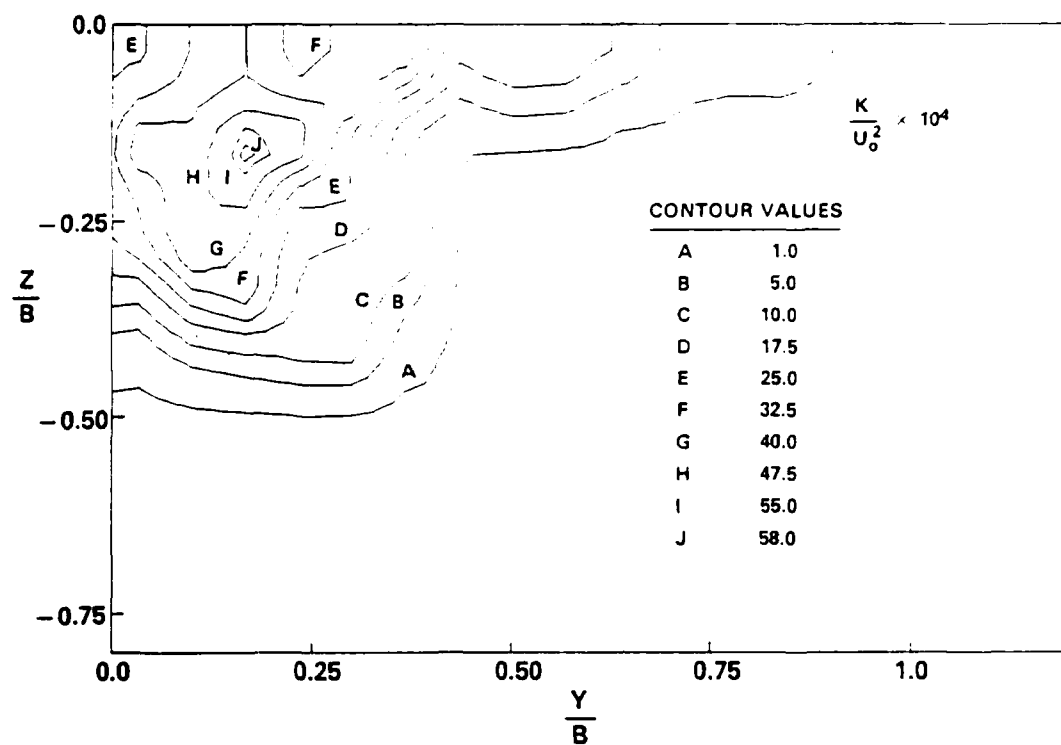
(b) $X = 16.0 \text{ ft}$

Fig. 9 - Contours of mean streamwise velocity: inboard rotation

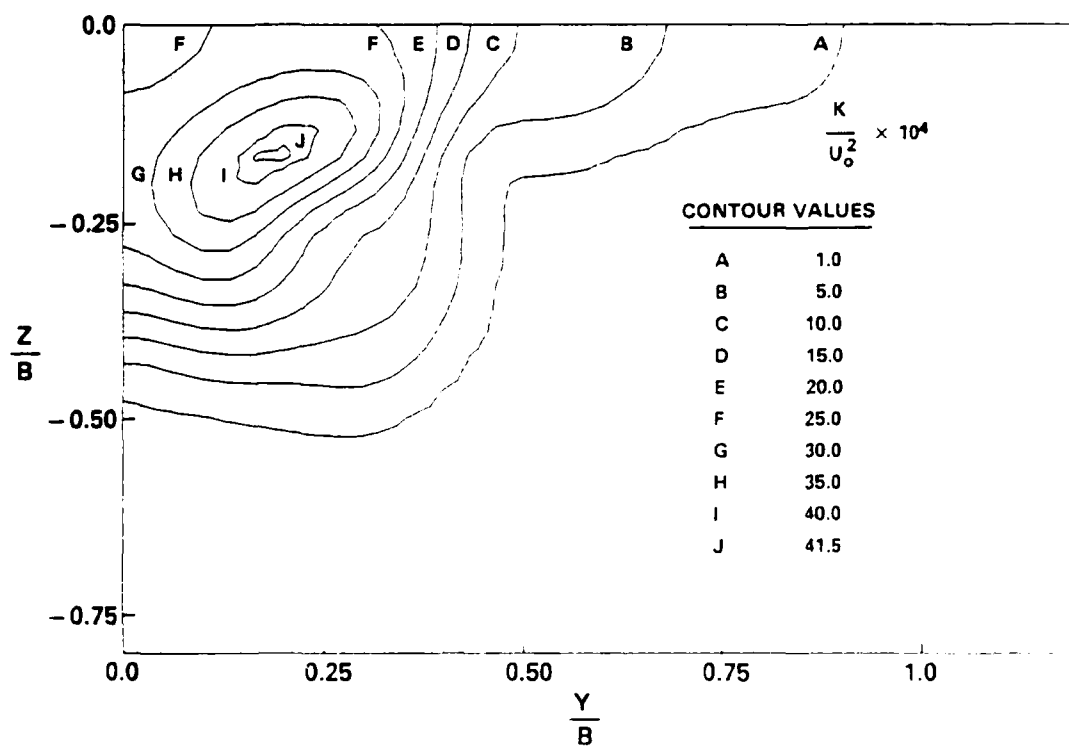


(c) $X = 30.0 \text{ ft}$

Fig. 9 (Cont'd) — Contours of mean streamwise velocity: inboard rotation

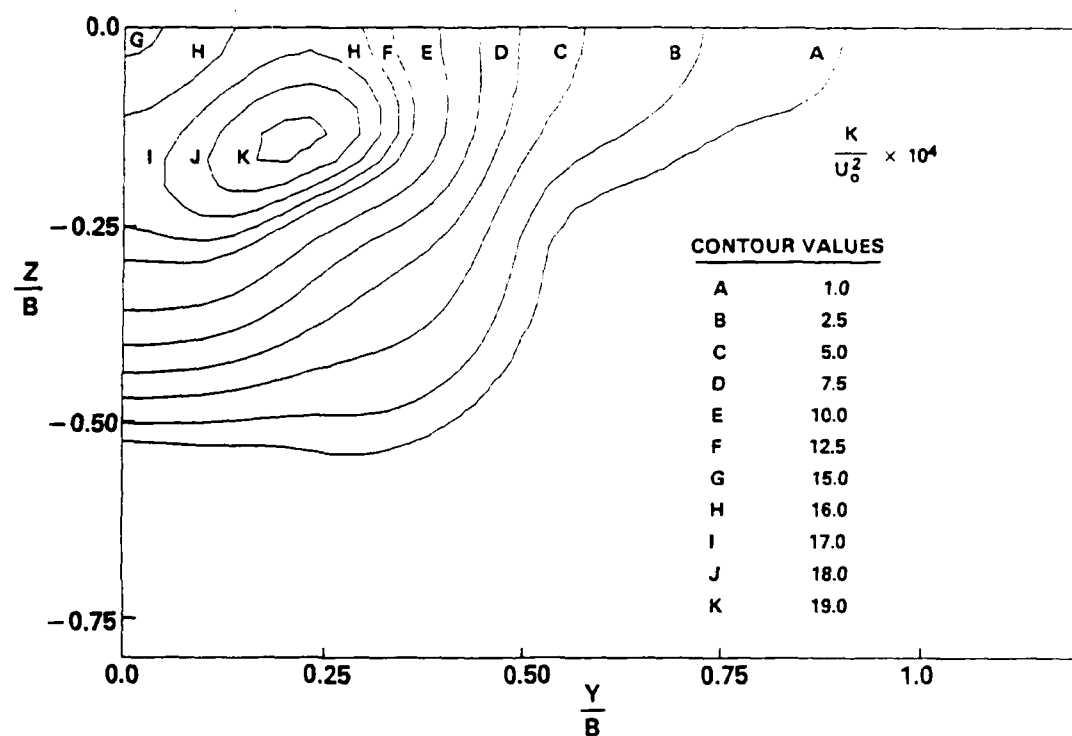


(a) $X = 10.0$ ft



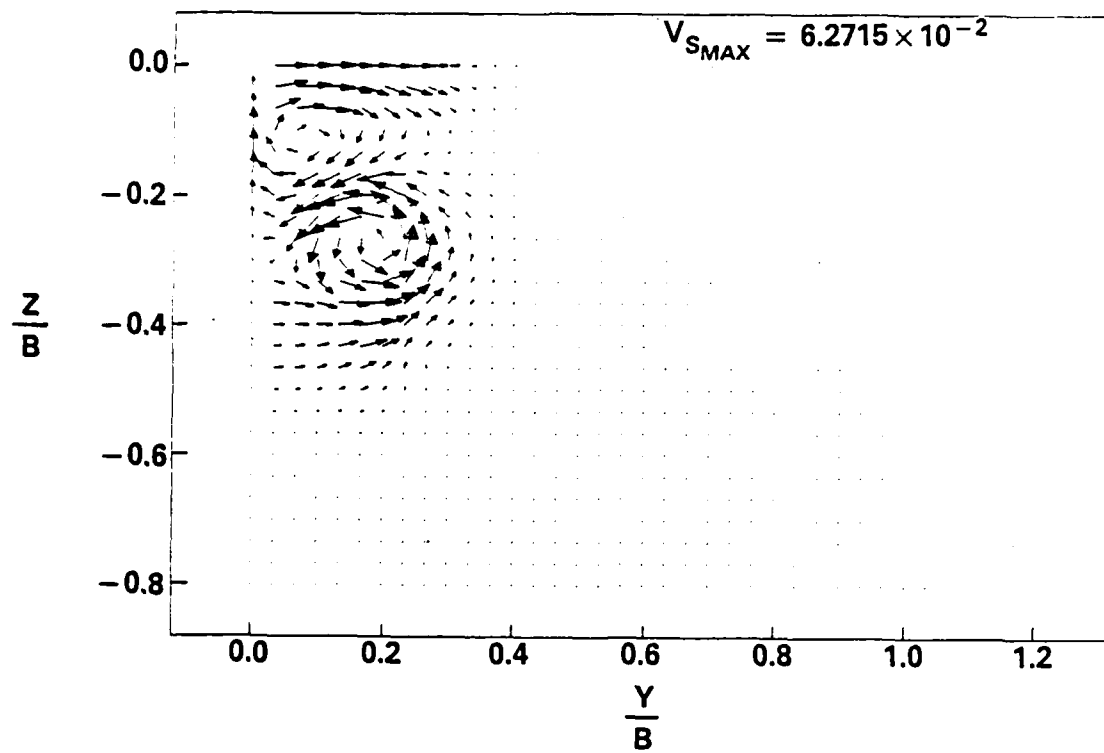
(b) $X = 16.0$ ft

Fig. 10 - Contours of turbulence kinetic energy: inboard rotation

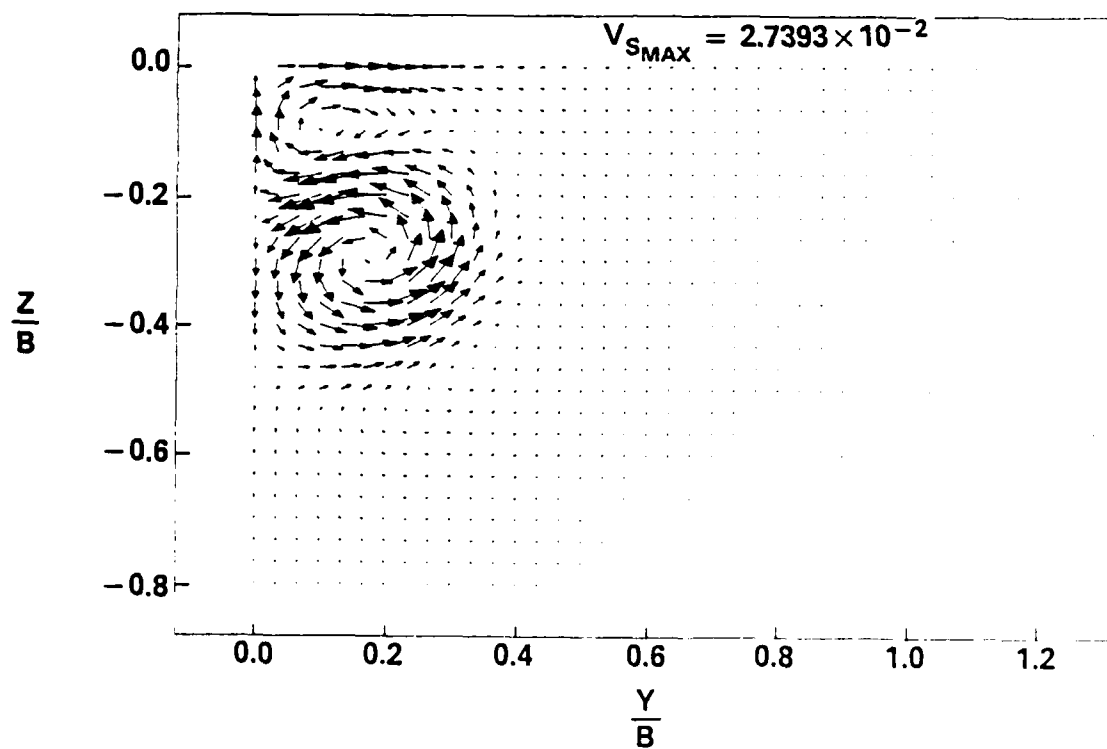


(c) $X = 30.0 \text{ ft}$

Fig. 10 (Cont'd) — Contours of turbulence kinetic energy: inboard rotation

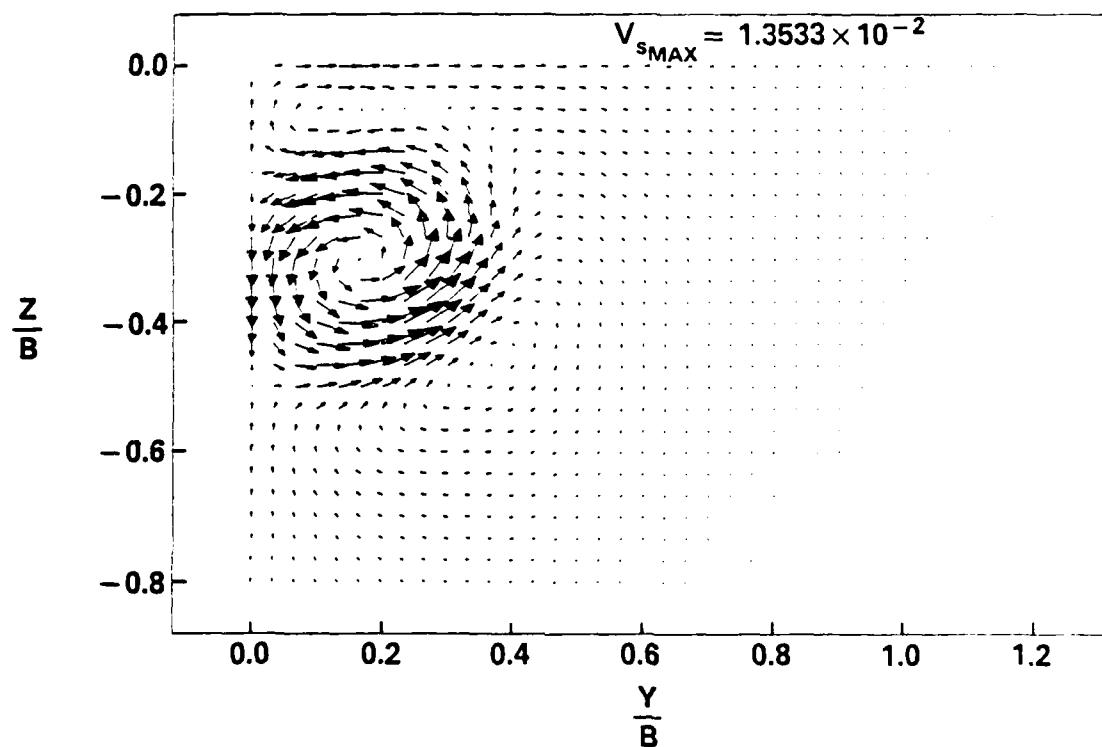


(a) $X = 10.0$ ft



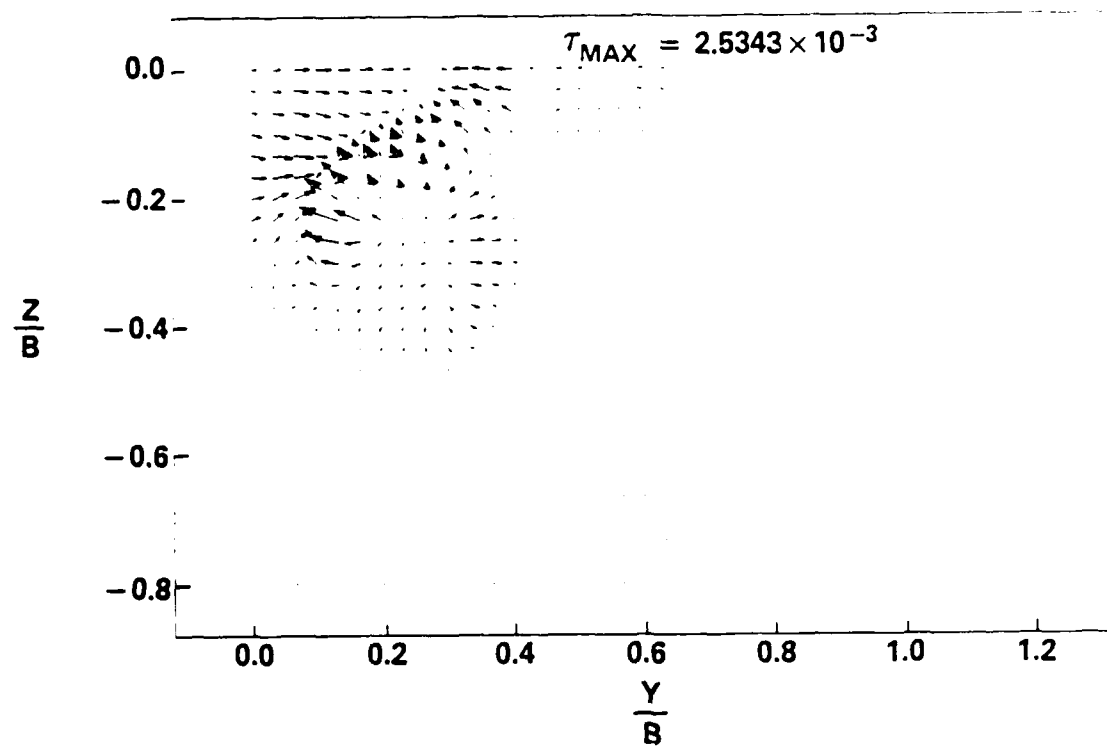
(b) $X = 16.0$ ft

Fig. 11 - Swirl velocity vectors: inboard rotation

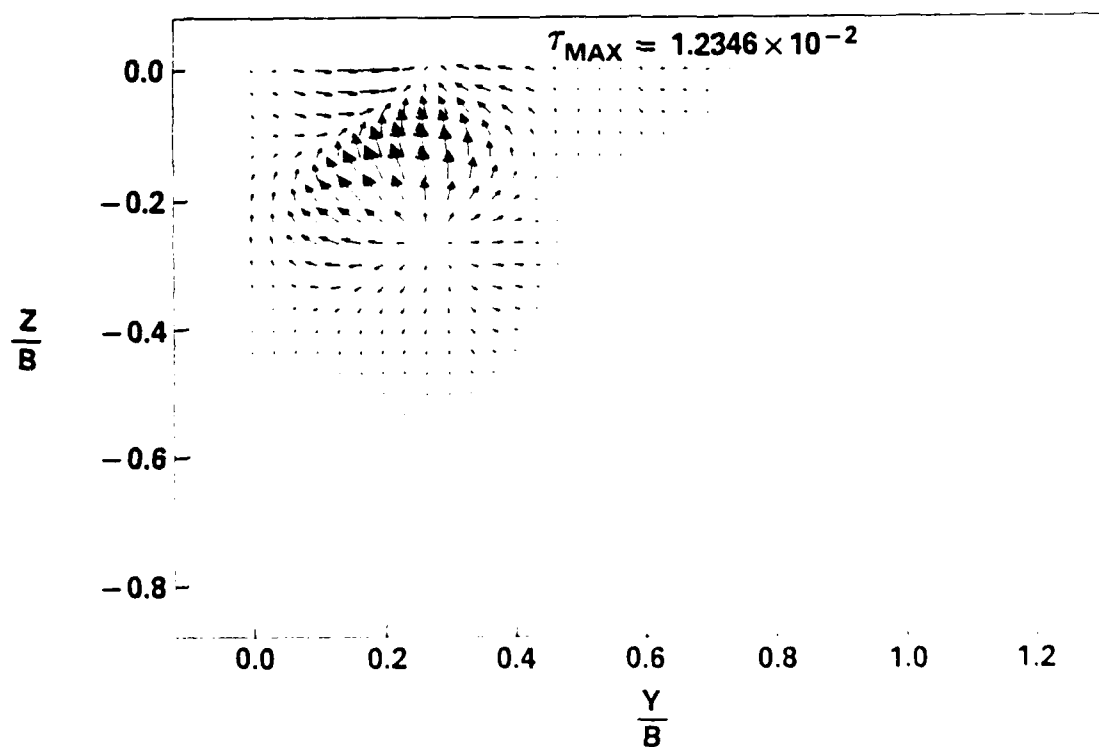


(c) $X = 30.0 \text{ ft}$

Fig. 11 (Cont'd) — Swirl velocity vectors: inboard rotation

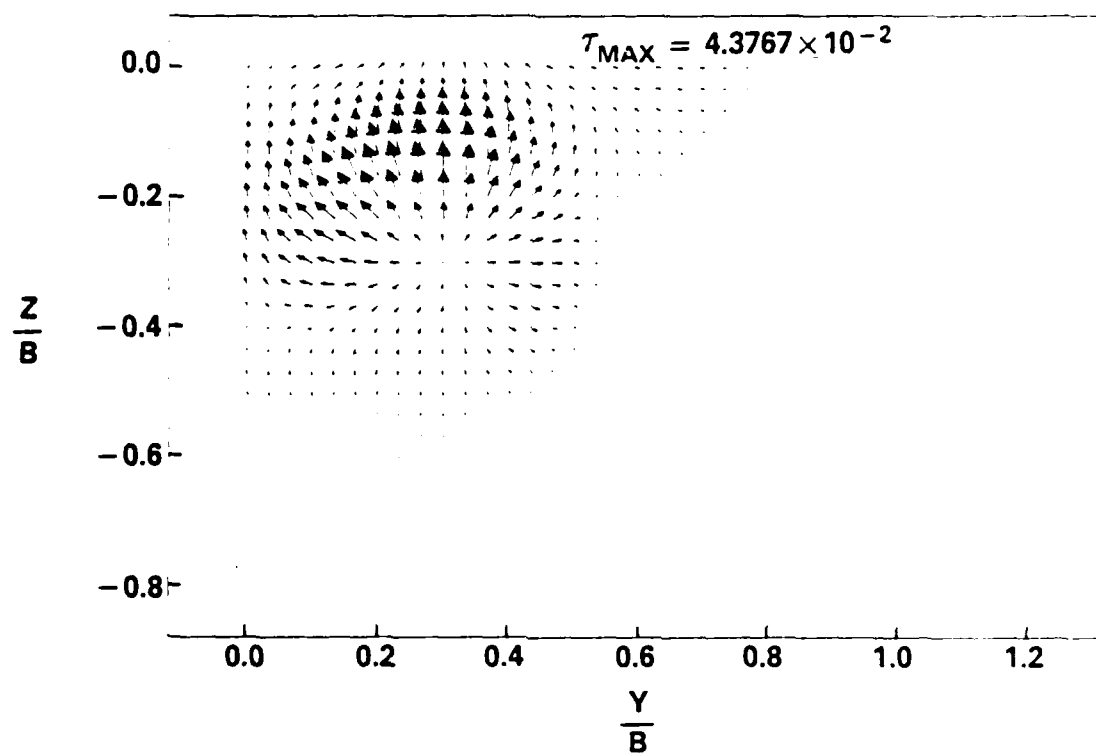


(a) $X = 10.0 \text{ ft}$



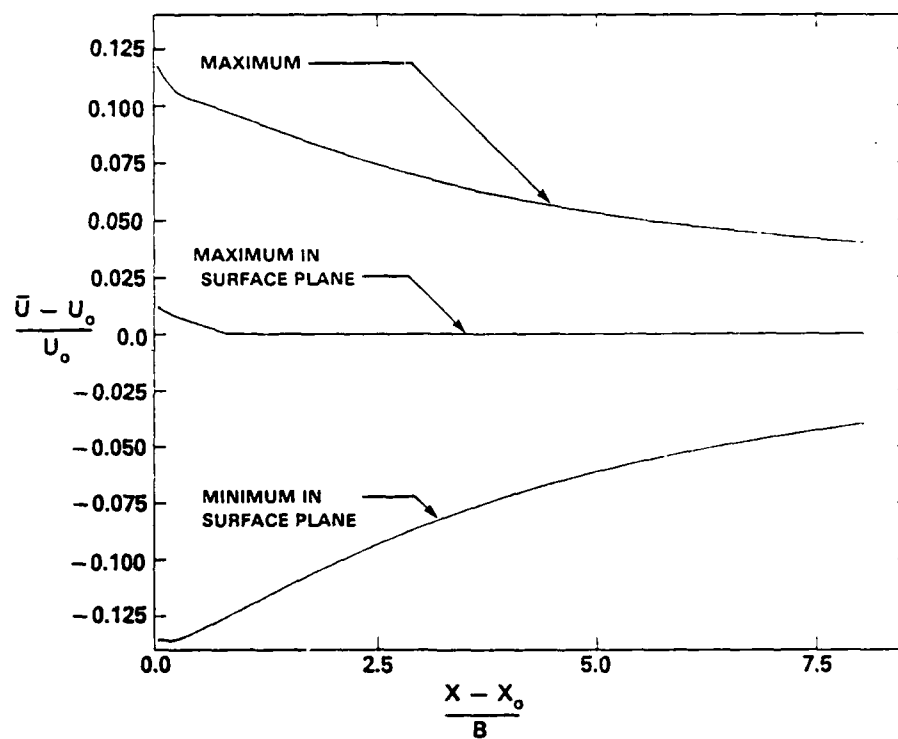
(b) $X = 16.0 \text{ ft}$

Fig. 12 - Reynolds stress distribution: inboard rotation

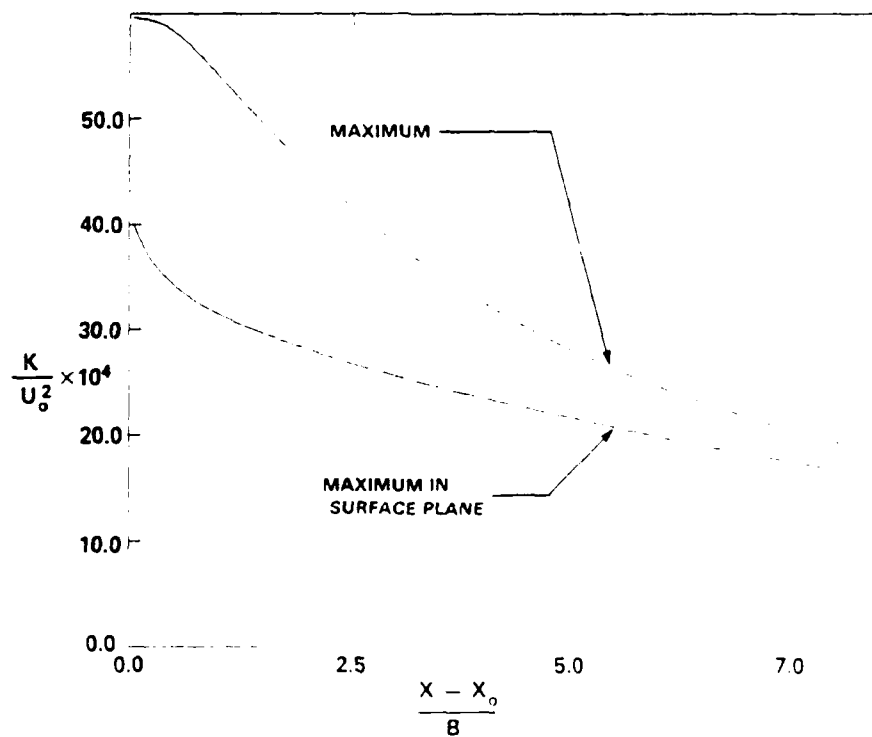


(c) $X = 30.0 \text{ ft}$

Fig. 12 (Cont'd) — Reynolds stress distribution: inboard rotation

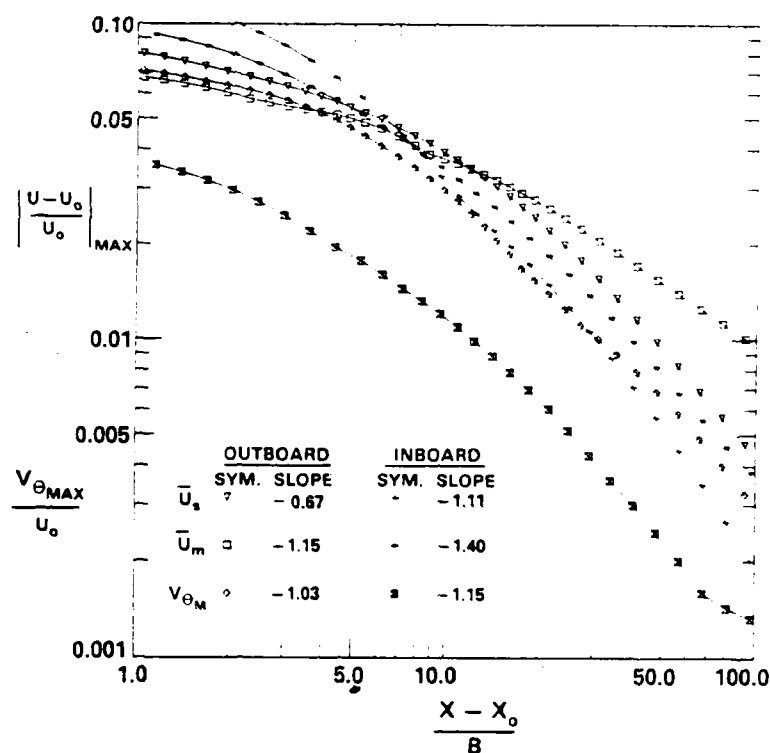


(a) streamwise velocity

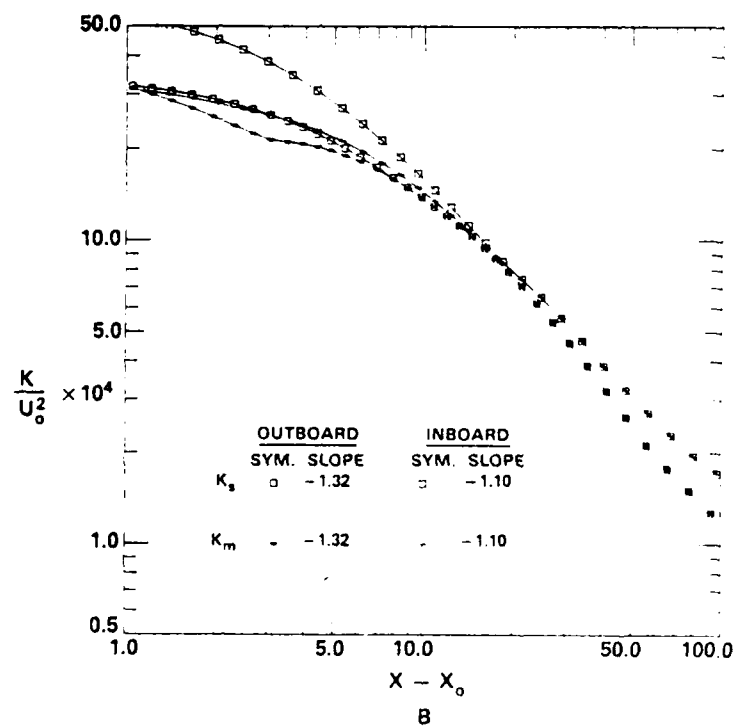


(b) turbulence kinetic energy

Fig. 14 - Axial decay of characteristic values of streamwise velocity and turbulence kinetic energy: inboard rotation



(a) velocity



(b) turbulence kinetic energy

Fig. 15 - Comparison of axial decay rates for inboard and outboard simulations:
 $(\cdot)_m$ = maximum, $(\cdot)_s$ = maximum in surface plane

END

FILMED

MARCH, 19 88

DTIC